Geophysical Journal International

Geophys. J. Int. (2026) **245,** 1–22 https://doi.org/10.1093/gji/ggag032
Advance Access publication 2026 January 24
Research Paper

Characterizing magnetic fabrics from ∼116 Ma old Salma dike, India: implication for magma flow direction

Ayanangshu Das [1] Rafał Szaniawski[1] and Katarzyna Dudzisz [2]

[1]*Institute of Geophysics, Polish Academy of Sciences, Ks. Janusza 64, 01-452 Warszawa, Poland. E-mail: ayanangshu.das@igf.edu.pl*
[2]*Karlsruhe Institute of Technology (KIT), Institute of Applied Geosciences, Adenauerring 20a, 76131 Karlsruhe, Germany*

Accepted 2026 January 16. Received 2026 January 12; in original form 2025 October 15

SUMMARY

Anisotropy of magnetic susceptibility (AMS) analysis is widely used as an efficient petrofabric tool to infer magma flow patterns within dikes. However, interpretations of magnetic fabric often get complicated by the occurrence of anomalous (intermediate/inverse) fabrics oriented normal to the dike plane, which may lead to uncertainty, unlike the straightforward normal fabrics along the intrusion plane. In this article, we present a detailed rock-magnetic and magnetic fabric study of India's ∼116 Ma old Salma dike, which is the most prominent and longest dike related to the early Cretaceous Rajmahal Trap (RT) volcanism. A joint analysis of in-phase and out-of-phase anisotropy of magnetic susceptibility (i.e. ipAMS and opAMS) and anhysteretic remanent magnetization (AARM) fabrics allowed us to identify the different sources of the observed fabric and subfabrics. Rock-magnetic analyses suggest that the magnetic mineralogy consists of at least two types of titanomagnetite with varying Ti-content. FORC suggests that the dike is dominated by PSD grains with varying influence from SD grains. The ipAMS fabric is primarily carried by SD grains of low-Ti titanomagnetite, while opAMS is governed by larger MD/PSD titanomagnetite with higher-Ti content. Results indicate that anomalous, intermediate-type ipAMS fabrics, particularly along the dike margins, are caused as a combined effect of SD grains, late-stage crystallization and mild high-temperature oxidation. At the dike centre, post-emplacement alteration, intense exsolution of the primary titanomagnetite and magma backflow are responsible for anomalous fabrics. In contrast, the majority of normal ipAMS, opAMS and AARM fabrics are coaxial, providing a reliable record of magma flow as confirmed from the long axes trend distribution of the plagioclase laths along the dike plane. These fabrics reveal a dominant subvertical magma flow direction during emplacement, indicating magma ascent from depth. Even though the magnetic fabrics do not unequivocally constrain the deeper processes underneath Moho, they are compatible with the idea of a subcrustal magmatic layer beneath the region, potentially originating from decompression melting or the influence of the Kerguelen plume, to be the feeder source.

Key words: Magnetic fabrics and anisotropy; Magnetic mineralogy and petrology; Rock and mineral magnetism; Large Igneous Provinces; Magma migration and fragmentation.

1. INTRODUCTION

Large Igneous Provinces (LIPs) are characterized by the massive outpouring of millions of km^3 of basaltic lava flows over a 1–3 Myr interval (J.J. Mahoney & M.F. Coffin 1997; Ernst 2014) due to tectonic rifting and/or mantle plumes. Continental Flood Basalts are frequently accompanied by dike swarms or sill complexes, usually reflecting the relics of fractures through which magma efficiently migrates towards the surface (e.g. A. Gudmundsson 1990, 2002; M.L. Curtis *et al.* 2008; X. Pan *et al.* 2014; A. Tibaldi 2015; R.E. Ernst *et al.* 2019; A. Das & J. Mallik 2020; A. Das *et al.* 2021). Magma emplacement within a dike is a reasonably complex phenomenon which depends on several factors, such as, local and regional tectonic stress pattern, occurrence of discontinuities providing possible channel for magma flow, volume of available magma, heat budget and buoyancy of magma, as well as many other processes. (M.I.B. Raposo & M. Ernesto 1995; M.I.B. Raposo & M.S. D'Agrella-Filho 2000; C.

Aubourg *et al.* 2002; M.I.B. Raposo *et al.* 2007; R. Ray *et al.* 2007; C. Kissel *et al.* 2010; J.Y.L. Woo & C.R.J. Kilbum 2010; G. Airoldi *et al.* 2011; X. Pan *et al.* 2014; E. Rivalta *et al.* 2015; L. Mantiloni *et al.* 2023; R. Shajahan *et al.* 2024, etc.). Magma flow in a dike may vary from vertical to lateral, depending upon the distance of the shallow/subcrustal feeder chamber (T. Mittal & M.A. Richards 2021) or deep source (B.A. Black & M. Manga 2017) as a direct or indirect consequence of plume head impingement at the base of the lithosphere. Therefore, understanding the intricacies of magma movement within a dike is significantly important to advance our understanding of the emplacement processes of any volcanic province (X. Pan *et al.* 2014).

From a methodological viewpoint, in addition to field observations (e.g. dike segmentation, elongated vesicles, mineral lineation) and shape-preferred orientation of minerals, anisotropy of magnetic susceptibility (AMS) is an efficient petro-fabric indicator (P. Rochette *et al.* 1992), which can be used to visualize the magma dynamics in dikes (e.g. L. Geoffroy *et al.* 2002; M. Wiegand *et al.* 2017; A. Das & J. Mallik 2020; A. Das *et al.* 2021; G. Shukla *et al.* 2024; R. Shajahan *et al.* 2024). This quick petrofabric technique relies upon the general assumption that ferromagnetic grains are preferentially aligned by the flow within the dike, with the maximum physical dimension along the flow direction. The corresponding magnetic foliation planes are subparallel or imbricated at a low angle to the dike plane, resulting in 'normal fabric' and are considered as a proxy for flow fabric (L. Geoffroy *et al.* 2002; M. Chadima *et al.* 2009). The standard AMS, that is, in-phase AMS (ipAMS), was successfully used to determine magma flow directions from dikes, such as the East Greenland dike swarm (J.-P. Callot & L. Geoffroy 2004), the Strietishvarf composite dike of East Iceland (P.I. Eriksson *et al.* 2011), the dikes of Azores (M.A. Moreira *et al.* 2015), the Deccan dike swarm (A. Das *et al.* 2021; G. Shukla *et al.* 2024), the dikes from the Mount Callana (R. Shahjahan *et al.* 2024) and others. In recent times, alongside the standard AMS (i.e. ipAMS), F. Hrouda *et al.* (2019) additionally applied the out-of-phase AMS (i.e. opAMS) to the Central Bohemian dike swarm of the Czech Republic to better distinguish between two magma pulses characterized by vertical feeding flow and late-stage lateral forceful magma injection.

In almost every study, several possible anomalous fabric configurations are reported that are often difficult to interpret in terms of primary flow fabric. These anomalous fabrics are often caused by several factors including, the single-domain grains (P. Rochette *et al.* 1992; E. Ferré 2002), distribution anisotropy of clustered ferrimagnetic grains (A. Stephenson 1994), complex magmatic or post-emplacement processes (e.g. late-stage crystallization, magma backflow, multiple magma pulses of contrasting composition etc.; H.B. Mattsson *et al.* 2011; B.S.G. Almqvist *et al.* 2012; F. Hrouda *et al.* 2019; S.A. Martin *et al.* 2019; A. Das & J. Mallik 2020) or by tectonic reasons (C. Soriano *et al.* 2007; P.I. Eriksson *et al.* 2014; V.K. Kusbach *et al.* 2019). Furthermore, mixed or composite fabrics, consisting of both normal and anomalous fabrics, can also result from crystallization of magnetic minerals during different stages of emplacement processes (P.F. Silva *et al.* 2014). However, such fabrics provide no reliable criteria for reconstructing the primary flow axis, and are discarded in most cases (C. Soriano *et al.* 2016). Therefore, rock-magnetic and petrographic observations must be integrated to better constrain the origin of the anomalous and mixed fabrics before characterizing them as flow-related.

In this study, we intend to focus on the NNW-trending, >50 km long Salma dike, which is the largest dike genetically associated with the Early Cretaceous Rajmahal Trap (RT) volcanism. There is an ongoing debate about the possible feeder chamber for the RT volcanism. M.R. Kapawar *et al.* (2021) studied the RT flow sequences and supported the inference made by J.J. Mahoney *et al.* (1983), suggesting the Comei-Cona suite in Tibet as the feeder source. On the contrary, A.P. Singh *et al.* (2004) interpreted the subcrustal high-density igneous layer to be a possible direct feeder source. Even though the dikes are considered the pathways for magma migration from the shallow or subcrustal chambers, the dikes associated with the RT are left largely unexplored. Thus, knowledge about the magma emplacement mechanism in the Salma dike is of utmost importance owing to its possibility of being one of the feeder dikes for RT emplacement. The Salma dike is well discussed in terms of geochemical aspects, but lacks any documentation regarding its rock-magnetic and magnetic fabric characteristics. The aim of this study is two-fold: (a) to characterize the origin of the magnetic fabrics in terms of the magnetic carriers, and (b) to check if the fabrics are representative of primary flow fabric or of late-stage processes. To achieve this goal, we used a combination of the magnetic fabric analyses (e.g. ipAMS, opAMS and anisotropy of anhysteretic remanence magnetization, i.e. AARM), various rock-magnetic methods and petrographic observations.

2. GEOLOGICAL BACKGROUND

The Indian plate witnessed intense intraplate mafic volcanism in the Cretaceous period, starting with the Rajmahal Trap (RT) emplacement in the early Cretaceous and Deccan volcanism in the late Cretaceous. In the first of the above-mentioned events, the Kerguelen plume is likely accountable for (i) the breakup of the Indian block from Australia–Antarctica; (ii) the emplacement of the Comei-Bunbury LIP and (iii) the emplacement of the RT in northeastern India (e.g. D.-C. Zhu *et al.* 2009; H.K.H. Olierook *et al.* 2016; W. Bian *et al.* 2019; W. Peng *et al.* 2022). On the Indian plate, the RT volcanics are distributed within the Paleoproterozoic Chhotanagpur Gneissic Terrain (CGT) and in the Shillong plateau NE of it (e.g. M.F. Coffin *et al.* 2002; J.S. Ray *et al.* 2005; R.K. Srivastava *et al.* 2005, 2014, 2019a, b, 2020, 2023; A. Ghatak & A.R. Basu 2011, 2013).

The CGT is intruded by mafic dike swarms of varying ages, ranging from Mesoproterozoic (A. Kumar & T. Ahmad 2007; R.K. Srivastava *et al.* 2012) to Late Cretaceous (R.K. Srivastava *et al.* 2014, 2020) (Fig. 1a). These dikes can be classified into the following three groups, (a) the ENE- to E-trending Mesoproterozoic mafic dikes intruding the Precambrian gneisses (R.K. Srivastava *et al.* 2012), (b) the NNW- to WNW-trending Early Cretaceous (ca. 118–109 Ma) dolerite dikes intruding the Gondwana sediments and Precambrian basement rocks (R.W. Kent *et al.* 2002; R.K. Srivastava *et al.* 2014, 2020, and 2023) and (c) the NNE- to NE-trending Late Cretaceous (ca. 70–65 Ma) dolerite dikes intruding the Gondwana sedimentary rocks (R.W. Kent *et al.* 2002; R.K. Srivastava *et al.* 2014, 2020). Along with the Early Cretaceous (ca. 118–103 Ma) dikes, the contemporaneous RT flows are recognized in the CGT (e.g. M. Storey *et al.* 1992; A.K. Baksi 1995; R.W. Kent *et al.* 1997; R.K. Srivastava *et al.* 2023). Discreet exposures of Late Cretaceous Deccan basalts are also evident at the western periphery of the CGT.

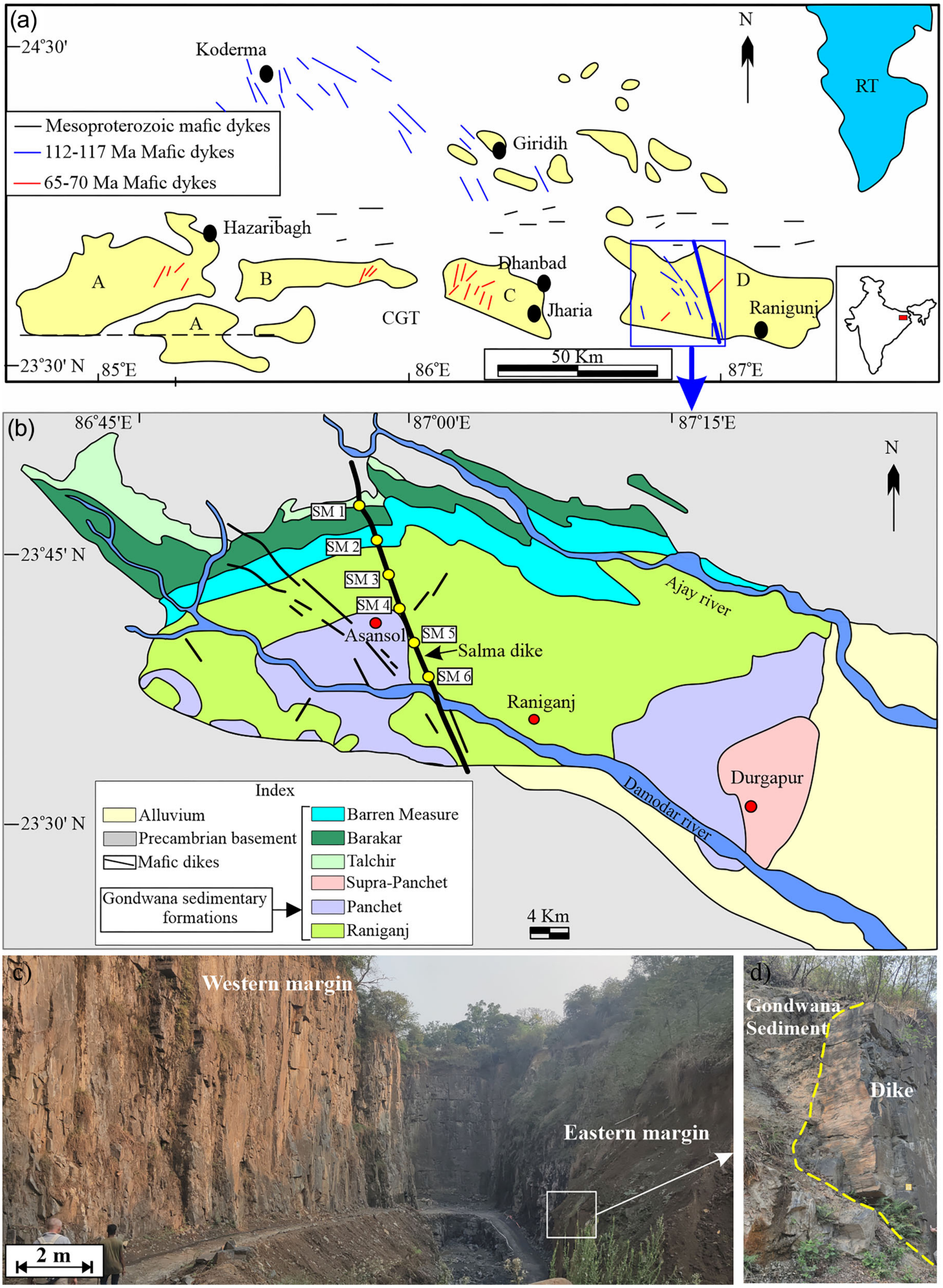

Figure 1. (a) Distribution of Mesoproterozoic and Cretaceous mafic dikes in the Chhotanagpur gneissic complex (modified after R.K. Srivastava *et al.* 2023). The letters A to D describe Gondwana sedimentary basins: Karanpura (A); Bokaro (B); Jharia (C) and Raniganj (D). The NW-trending Salma dike (marked with a blue bold line in Fig. 1a) is chosen as the target for this study, and a rectangle demarcates the study area. (b) Geological map of the Raniganj Basin exhibiting the distribution of mafic dikes (modified after R.K. Srivastava *et al.* 2019a). The studied Salma dike is exhibited in bold, and sampling locations are marked. (c) and (d) field photographs of Salma dike outcrop showing its massive width and border with Gondwana sediments.

The Early Cretaceous NNW to WNW-trending dolerite dikes are distributed over the Raniganj, Giridih and Koderma region (Figs 1a and b). In the Giridih and Koderma areas, the dikes intrude only Precambrian basement rocks. The dolerite dikes of the Raniganj basin mostly cut through the Gondwana sedimentary rocks hosting coal beds (Fig. 1b). However, the NNW trending Salma dike, that is, the subject of this study, also intrudes the Precambrian basement rocks along with the coal bearing Gondwana sedimentary rocks (Figs 1b and d).

Despite being the largest dike associated with the RT, the existing state of knowledge on the Salma dike is rather limited. The palaeomagnetic directions from the Salma dike, reported by S.K. Patil & B.R. Arora (2008), are consistent with the RT lava flows. The Salma dike is geochemically coherent with the geochemistry of the mafic volcanics related to the Greater Kerguelen LIP (R.K. Srivastava *et al.* 2019a). The $^{40}Ar/^{39}Ar$ whole-rock geochronometric dating conclusively reported an age of ca. 116 ± 1.4 Ma, implying its linkage with the Kerguelen plume (R.K. Srivastava *et al.* 2019a, b, 2023).

3. SAMPLING AND METHODOLOGY

3.1 Sampling

Fifty-one oriented block samples were collected from nine sites distributed over six sampling locations of the Salma dike to understand its magma flow dynamics. In general, the dike is exposed in stone quarries from North to South. The samples were collected from nine sites at six locations along the dike trend from North to South (Fig. 1b). The interval of the six sampling locations and the distribution of the nine sampling sites are shown in Section S2 of the supplementary material. A. Das & J. Mallik (2020), from their study of the Deccan dikes, recommended collecting samples from the margin of thick dikes as inconsistent fabric was observed at the central part owing to rather slow cooling rate and lack of shear stress (e.g. M.D. Knight & G.P.L. Walker 1988; C. Constable & L. Tauxe 1990; E. Cañon-Tapia 2004; E. Cañon-Tapia & E. Herrero-Bervera 2009; C.I. Caballero-Miranda *et al.* 2016, etc.) compared to the margin. Moreover, the local convection and associated backflow can obliterate the flow-derived fabric in the central part. Therefore, the majority of the samples were collected from both margins of the Salma dike. All the samples were collected within 3 m of the dike margin with an approximate interval of 0.5 m. However, six samples were collected from the centre of the dike at one location to check the consistency of fabric across the dike. Multiple cylindrical core specimens with 22 mm height and 25.4 mm diameter were drilled out from each of the dike samples. AGICO Inc. orientation standards protocol (https://www.agico.cz/downloads/documents/agicoprints/orpar.pdf) was followed to orient the specimens. All the laboratory measurements were carried out in the Paleomagnetic Laboratory, Institute of Geophysics Polish Academy of Sciences, Warsaw.

3.2 Rock-magnetic analyses

In order to identify the constituting magnetic minerals of the Salma dike, several susceptibility- and magnetization-related rock-magnetic measurements were carried out.

3.2.1 *Magnetic susceptibility-related measurements*

Magnetic susceptibility (k) is a dimensionless quantity in the SI system, and we will use it throughout the paper. Both low- and high-temperature dependent susceptibility (k–T) analyses were carried out in air for nine samples using a KLY-5S Kappabridge with a CS4 high-temperature unit (Agico Inc., Czech Republic). Low-temperature variation of susceptibility was measured between −194°C and 0°C. High-temperature variation of susceptibility was measured during heating and subsequent cooling between 50°C and 700°C with the 400 Am^{-1} field intensity and 1220 Hz field frequency. The data were processed using Cureval8 software. The Curie temperature was determined using the peak tangent method (P. Lied *et al.* 2020).

The field-dependent variation of susceptibility was measured within fields ranging from 5 to 700 Am^{-1} at the operating frequency of 1220 Hz using the KLY5 Kappabridge on seven samples. The field-dependent susceptibility variations were characterized by the parameter k_{Hd} per cent, defined by a formula modified after H. De Wall (2000) as follows: k_{Hd} per cent = $[(k_{400}-k_{40})/k_{400}] \times 100$ per cent.

The presence of superparamagnetic grains was checked by measuring frequency-dependent susceptibility. The low- and high-frequency susceptibilities (i.e. k_{lf} and k_{hf}, respectively) were measured at 976 and 15 616 Hz frequencies using an MFK1 Kappabridge (Agico Inc., Czech Republic). Subsequently, frequency-dependent susceptibility (i.e. $k_{fd} = k_{lf} - k_{hf}$) and its percentage (i.e. using the formula calibrated for kappabridge with correction parameter 0.8 as follows k_{fd} per cent = $0.8 \times [(k_{lf}-k_{hf})/k_{lf}] \times 100$) (F. Hrouda 2011) were calculated.

3.2.2 *Magnetization-related measurements*

The thermal demagnetization of the three axes Isothermal Remanent Magnetization (IRM) or Lowrie test (W. Lowrie 1990), for seven samples was conducted. All the studied samples were magnetized along three orthogonal directions (x: 0.12 T, y: 0.4 T and z: 3.0 T) using the MMPM10 pulse magnetizer (Magnetic Measurements, UK) and then stepwise thermally demagnetized up to 600°C using the MMTDSC thermal demagnetizer (Magnetic Measurements, UK). The IRM was measured using a JR6 spinner magnetometer (AGICO Inc., Czech Republic). The IRM acquisition curve for eight samples (weight < 0.01 gm) from the dike were measured up to 500 mT. Subsequently, the D.P. Maxbauer *et al.* (2016) method for decomposition of the IRM curves was applied by the MAX UnMix web application to separate the magnetization components. Then the mean coercivity ($B_{1/2}$) corresponding to the half of the SIRM, and the dispersion parameter (DP) representing the dispersion of the cumulative log-normal distribution were calculated for each unmixed component. Selected samples were used to measure the hysteresis loop and back-field curves to constrain the magnetic domain state. All the hysteresis loops started from zero applied field. The dia/paramagnetic correction was performed over 70 per cent of the highest applied field, followed by the determination of the following parameters: coercivity (B_c), saturation magnetization (M_s) and saturation remanent magnetization (M_{rs}). The coercivity of remanence (B_{cr}) was determined from the backfield curve. Finally, a Day-Dunlop plot (R. Day *et al.* 1977; D.J. Dunlop 2002) was prepared using these determined parameters. Moreover, the FORC of selected samples was measured using an averaging time of 150 ms and a saturation field of 0.6 T. In total, 200 curves were measured and then processed, smoothed and drawn using FORCINEL software (R.J. Harrison & J.M. Feinberg 2008; R. Egli 2013). All these measurements were carried out using a MicroMag AGM (Princeton Instruments Corp., USA).

3.3 Petro-fabric analyses

3.3.1 Anisotropy of magnetic susceptibility (AMS) analyses

Both ipAMS and opAMS were measured simultaneously using the AGICO (Czech Republic) made KLY-5 Kappabridge. The computational processes for both the ipAMS and opAMS ellipsoids are the same. The AMS parameters such as bulk/mean susceptibility ($k_m = (k_1 + k_2 + k_3)/3$), magnetic foliation (F; k_1–k_2 plane), magnetic lineation (L; the attitude of k_1) (M.A. Khan 1962), corrected degree of anisotropy ($P_j = \exp.\{2[(\ln k_1 - \ln k_m)^2 + (\ln k_2 - \ln k_m)^2 + (\ln k_3 - \ln k_m)^2]\}^{1/2}$) and shape parameter ($T = [\{2\ln(k_2/k_3)\}/\ln(k_1/k_3)] - 1$ which ranges between +1 for oblate to −1 for prolate fabric) (V. Jelinek 1981) were calculated. The theory of the ipAMS and opAMS is described in Section S1 in the Supplementary Material.

3.3.2 Anisotropy of anhysteretic remanent magnetization (AARM) analyses

Cylindrical specimens, initially used for AMS study, were imparted with the anhysteretic remanent magnetization in six different directions in alternating fields up to 80 mT and DC field of 500 μT using the LDA5 unit (Agico Inc., Czech Republic), and it was measured with a JR-6A automatic spinner magnetometer (Agico Inc., Czech Republic). The AARM ellipsoid was calculated and visualized using the Anisoft5 software (M. Chadima & V. Jelínek 2008).

3.4 Petrography and image analysis

Microscopic investigations were conducted on the thin sections prepared from the samples collected from the dike margins and centre to observe the basic mineralogy. Two oriented thin sections from the dike margins and one from the dike centre were prepared along the dike plane (i.e. along the k_1–k_2 plane of the normal ipAMS and opAMS fabric) to document the long-axis trend distribution of the elongated plagioclase laths. The oriented photomicrographs were processed in grey scale, and the long-axis trend distribution of the plagioclase laths was measured using ImageJ (W.S. Rasband 2012). Rose diagrams were plotted using the GeoRose (https://www.yongtechnology.com/georose/) software.

4. RESULTS

4.1 Rock-magnetic analyses

4.1.1 Magnetic susceptibility-related measurements

The high-temperature *k–T* curves exhibit a stable Curie temperature between 540°C and 580°C in all of the samples (Figs 2a–d). All samples exhibit a second Curie temperature between 440°C and 480°C except for SM11, which shows a drop in the signal at 300°C (Fig. 2a). A drop in the signal is also evident in sample SM21 at ∼280°C (Fig. 2b). All such Curie temperatures correspond to different Ti content of the titanomagnetite. The typical shape and Curie temperatures ranging from 540°C–580°C suggest very low-Ti titanomagnetite. The Curie temperatures between 425°C and 480°C indicate the presence of titanomagnetite with comparatively higher Ti content. The drop of signal at ∼300°C temperature either suggests high-Ti titanomagnetite or can also be due to the transition of single-domain magnetite to a superparamagnetic state (Q. Zhang & E. Appel 2023) or annealing effect (M. Jackson & J. Bowles 2018). The corresponding low-temperature counterparts of the *k–T* curves are devoid of any Verwey transition, which implies > 3.5 atomic per cent of Ti (A. Kosterov *et al.* 2009; K. Dudzisz *et al.* 2022). The shape of the heating and cooling curves is irreversible and lacks a second Curie temperature at ∼470°C on the cooling curve in most samples, except for SM11. However, two samples (e.g. SM21 and SM3-10) show enhanced susceptibility values during cooling compared to heating (Figs 2b and c), most likely due to thermochemical transformation to some new ferrimagnetic phases due to thermal treatment. It is worth noting that Curie temperatures derived from cooling runs are usually lower than those of the heating curve.

The weak field-dependence of in-phase magnetic susceptibility (ipMS) is characterized by k_{Hd} per cent < 1 per cent in all the studied samples except for sample SM214, where k_{Hd} per cent is ∼2 per cent (Fig. 2e). The out-of-phase magnetic susceptibility (opMS) demonstrates significant variation with an applied field, as evident from the corresponding k_{Hd} per cent (Fig. 2f). The opMS k_{Hd} per cent is greater than 16 per cent in all samples, with a maximum of ∼52 per cent in SM21. Pure magnetite is virtually field-independent, unlike titanomagnetite (F. Hrouda *et al.* 2019). Therefore, the weak field dependence of ipMS suggests titanomagnetite with very low-Ti content. Moreover, it is worth noting that the ipMS is about two or three orders of magnitude higher than the opMS, as evident in Figs 2(g) and (h). The opMS of titanomagnetite is non-zero, unlike magnetite (F. Hrouda *et al.* 2019). So, the lower value of opMS and its comparatively strong field dependence suggest titanomagnetite with relatively higher Ti content.

Additionally, k_{fd} per cent varies between 0.7 and 1.2 per cent with mean and median at 0.97 per cent and 0.91 per cent respectively. Such low values of k_{fd} per cent (<1.5 per cent) indicate almost no or negligible content of superparamagnetic particles in the samples (Table 2).

4.1.2 Magnetization-related measurements

The thermal demagnetization of three-component IRM demonstrates the dominance of a soft-coercivity component consistently along the Salma dike (Figs 3a–d). In some samples, a small contribution of intermediate fractions can be observed (Figs 3a, d). Most of the samples show a slight drop in magnetization between 300°C and 330°C, except for location SM6, where the drop is much more prominent. All samples show an unblocking temperature at ∼500°C, followed by a maximum unblocking temperature of ∼550°C–580°C (Fig. 3). The observed unblocking temperatures at ∼300°C, 500°C and ∼550°C–580°C indicate the occurrence of titanomagnetite with varying Ti content.

The IRM acquisition curves for all the samples are similar and attain saturation well below 200 mT (Fig. 3e), indicating

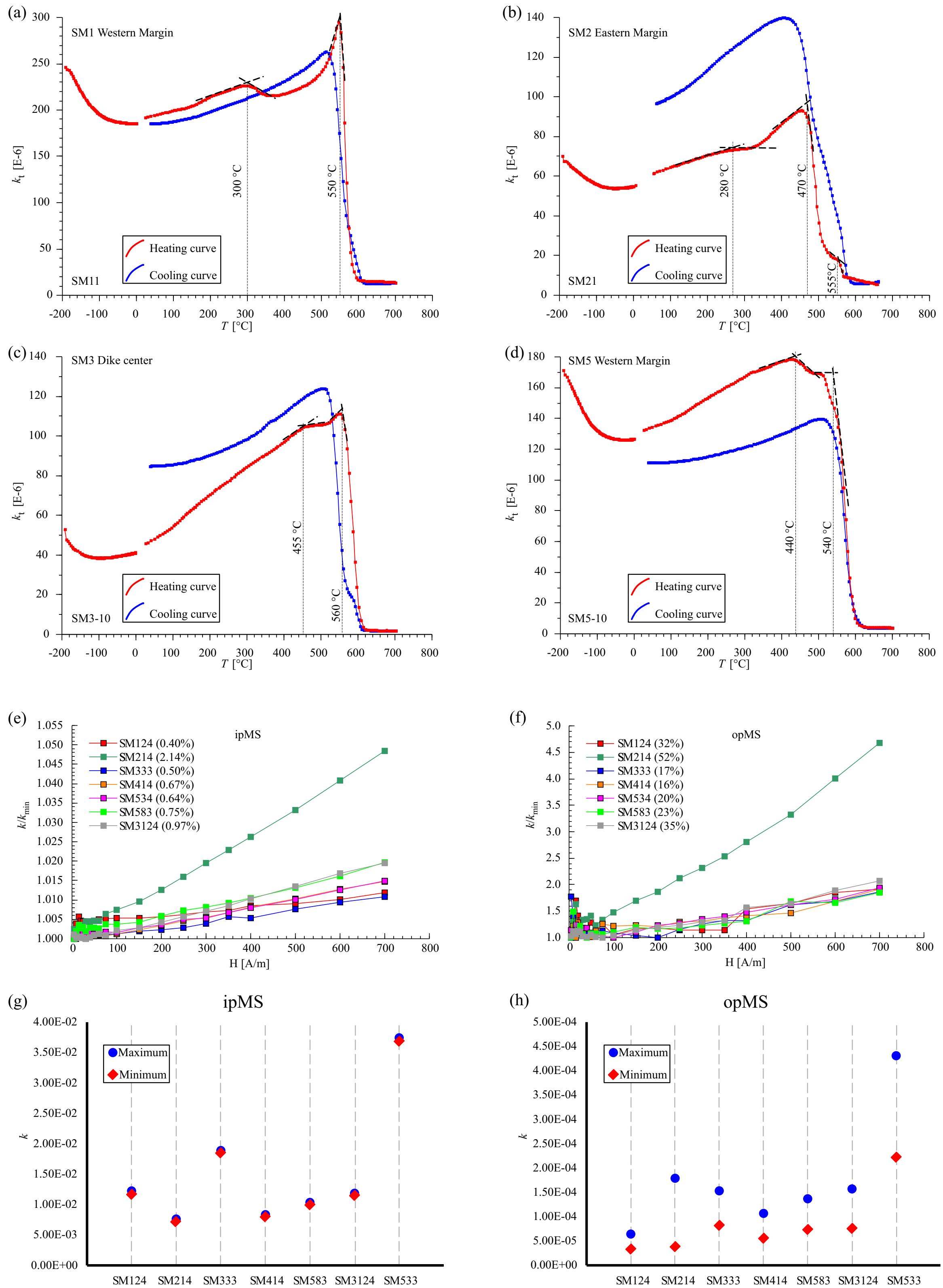

Figure 2. Results of the susceptibility-related rock-magnetic measurements of the Salma dike: (a)–(d) Temperature-dependent susceptibility measurement. The data for the rest of the samples are shown in Fig. S3 in Section 3 of the attached supplementary material. (e)–(f) Field-dependent susceptibility variation of ipMS and opMS, respectively. k_{Hd} per cent are shown against the corresponding sample number. (g)–(h) maximum and minimum ipMS and opMS, respectively.

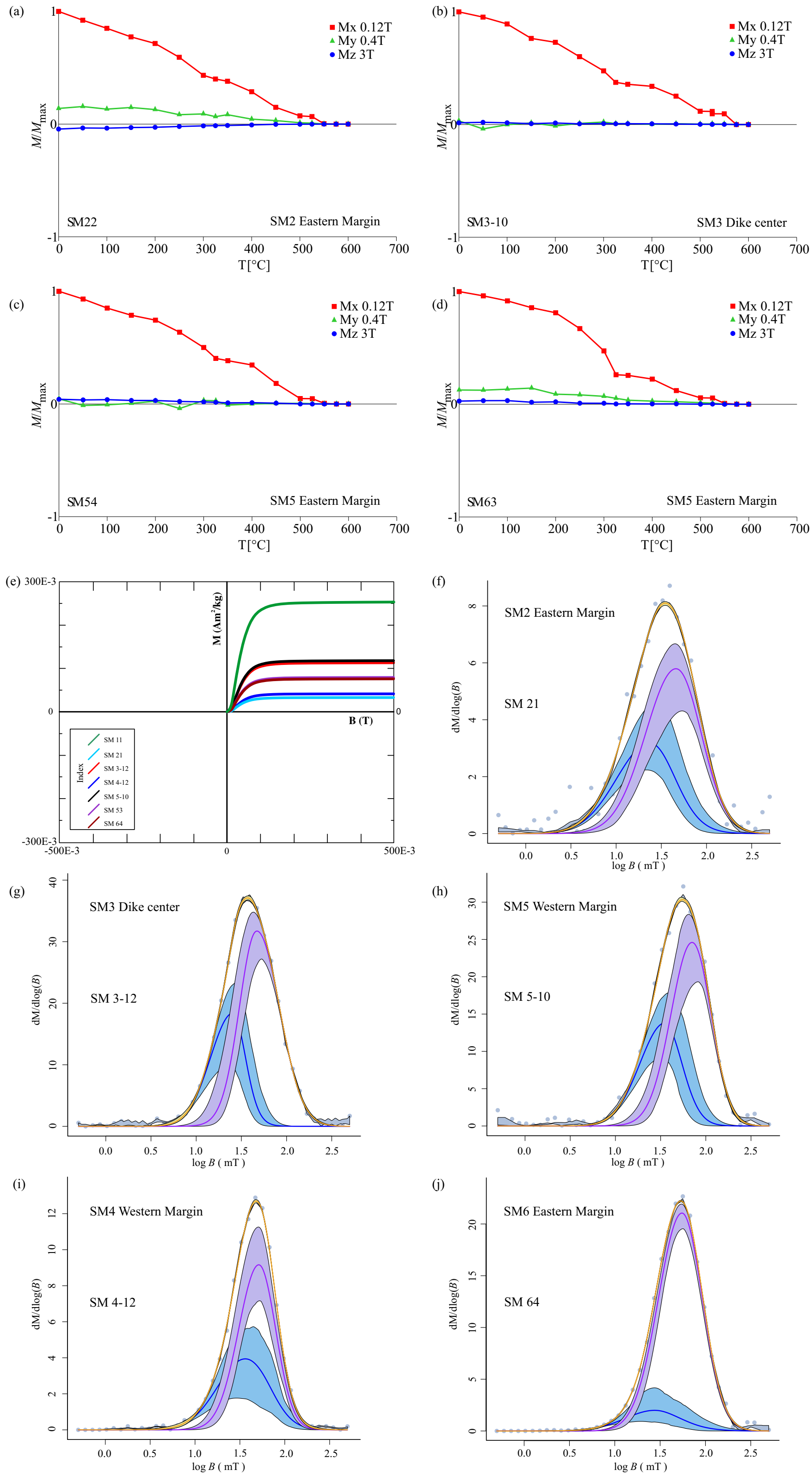

Figure 3. Results of the magnetization-related rock-magnetic measurements of the Salma dike: (a)–(d) Thermal demagnetization of three-Axes IRM. The data for all the studied samples are shown in Fig. S4 in Section 3 of the attached supplementary material; (e) IRM curves; (f)–(j) IRM component analysis using the MAX UNMIX web application (D.P. Maxbauer *et al.* 2016) with the following colour coding: violet—component 2, blue—component 1, Yellow—sum of the two components, and grey—data points.

Table 1. Table presenting the IRM component analysis and hysteresis parameters. $B_{1/2}$ = Mean Coercivity; DP = Dispersion parameter; M_s = Saturation Magnetization; M_r = Remanence magnetization; B_c = Coercivity; B_{cr} = Coercivity of remanence.

Sample	Component 1				Component 2				M_s(mAm^2 kg^{-1})	M_r(mAm^2 kg^{-1})	B_c(mT)	B_{cr}(mT)	Ferro/Para content (per cent)
	Contribution (per cent)	Log($B_{1/2}$)(mT)	$B_{1/2}$(mT)	DP(Log unit)	Contribution (per cent)	Log($B_{1/2}$)(mT)	$B_{1/2}$(mT)	DP(log unit)					
SM1-1	22.6	1.4	27.9	0.17	77.4	1.7	54.3	0.19	915.7	282.6	21.98	31.09	96.99
SM2-1	36.8	1.3	20.1	0.33	63.2	1.6	41.2	0.30	284.6	45.62	11.46	17.68	92.56
SM2-5	20.8	1.4	26.1	0.18	79.2	1.7	53.9	0.18	187.0	69.06	24.07	33.66	92.28
SM3-12	33.6	1.3	20.8	0.19	66.4	1.7	52.9	0.22	761.3	136.1	15.07	22.74	96.85
SM4-12	37.5	1.5	33.1	0.29	62.5	1.7	47.9	0.20	220.6	53.44	17.60	27.41	92.04
SM5-1	37	1.5	29.8	0.23	63	1.8	66.9	0.22	595.8	136.7	20.62	34.54	95.97
SM5-3	25.4	1.4	27.9	0.19	74.6	1.7	52.9	0.18	245.9	88.38	23.23	32.33	94.21
SM6-4	10.7	1.4	24.9	0.31	89.3	1.7	51.6	0.24	324.4	78.93	20.28	32.68	94.31

the predominance of low-coercivity phases such as titanomagnetite, which is consistent with the results obtained from the magnetic susceptibility-related rock-magnetic methods. Regardless of sampling positions on the dike, all the samples demonstrate the existence of two components that are heavily overlapping with each other:

(a) The first component (i.e. C1) is a relatively soft component depicting a mean coercivity range between 20–33 mT and the dispersion parameter (DP) range between 0.17 and 0.33 (log units) (Figs 3f–i; Table 1). The contribution of such a component mostly varies between 20 and 37 per cent except for the sample SM64, where the contribution is ~10 per cent (Fig. 3j).

(b) The second component (i.e. C2) manifests comparatively higher coercivity range between 41 and 67 mT with dispersion parameters range of 0.18–0.30 (Figs 3f–i; Table 1). This component seems to be the major dominating phase contributing up to 69–77 per cent of the observed IRM, except for the sample SM6-4, where C2 itself contributes 90 per cent (Fig. 3j).

According to K. Dudzisz *et al.* (2022), C1 and C2 fall within the range of titanomagnetite (likely exsolved) with intermediate and very low-Ti content, respectively.

All the samples exhibit rather narrow-waisted hysteresis loops (Fig. 4a), suggesting a mixture of magnetic minerals with different coercivities and/or grain sizes. After removal of paramagnetic effect, the remanent magnetization (M_r) and saturation magnetization (M_s) fall within a wide range between 45 and 282 and 187–915 mAm^2 kg^{-1}, respectively. The ferromagnetic phase is also characterized by low coercivity (B_c) ranging from 11 to 24 mT, with an average of about 19.28 mT. On the other hand, the coercivity of remanence (B_{cr}), obtained from the backfield curve spanning between 17 and 34 mT, gives rise to an average value of ~29.02 mT. Ferro/para content estimated from the initial slope of the uncorrected and corrected hysteresis loop suggests that the ferromagnetic contribution to the total magnetic susceptibility of the sample is significantly high (>90 per cent). Therefore, the results obtained from hysteresis loop measurements of the samples are in line with the other rock-magnetic analyses, indicating that the ferromagnetic minerals like titanomagnetite with variable Ti content dominantly contribute to the magnetic susceptibility. Moreover, the Day-Dunlop plot (Fig. 4b; R. Day *et al.* 1977; D.J. Dunlop 2002) suggests that the data points fall outside any of the fields for pure multidomain (MD), pseudo-single domain (PSD) and single domain (SD). However, the distribution of the majority of data points plots along the SD–MD mix curve for magnetite (D.J. Dunlop 2002).

FORC analysis of selected samples (Figs 4c–k) indicates the presence of grains in PDS (vortex) state with an SD tail continuing along the central ridge up to 150 mT (sample SM64 up to 200 mT). The outer contours displayed a characteristic divergent asymmetric pattern with mainly closed inner contours around a coercivity peak at 10–50 mT (SM64 up to 100 mT). Sample SM21, as the sole, has open contours that indicate a more MD-like type of grains (Fig. 4d). The FORCs are asymmetrical, and the slight upward offset seems to indicate the presence of non-interacting magnetic grains (A.P. Roberts *et al.* 2000).

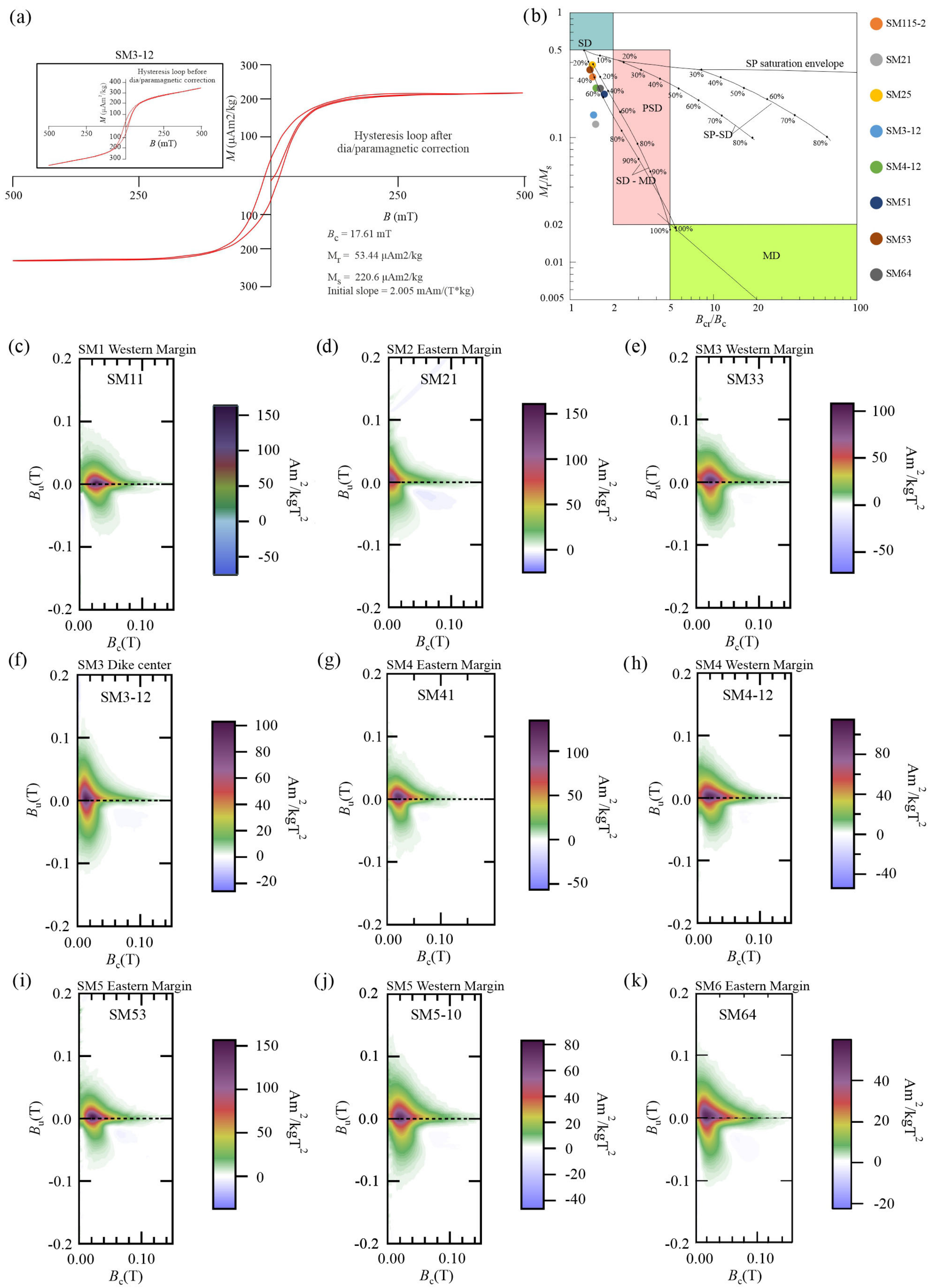

Figure 4. (a) The hysteresis loops of one representative sample. The inset shows the hysteresis loop before dia-/paramagnetic correction. (b) Day-Dunlop plot prepared for all the samples using the hysteresis and backfield parameters. (c)–(k) FORC diagrams prepared using FORCINEL software.

4.2. Petro-fabric analyses

4.2.1 AMS analyses

The mean parameters and directions of the principal susceptibility axes obtained from AMS analyses on a total 51 samples collected from nine sites distributed over six selected locations on the Salma dike, are presented in Fig. 5, Table 2 and Tables S1 and S2 attached in the Supplementary Material. Stereonet plottings of individual samples from the marginal part, along with the spatial distance from the dike margin, are shown in Fig. S5 (ipAMS) and Fig. S6 (opAMS) in the Supplementary Material. The ipAMS mean susceptibility (k_m) values are high and range from 6.88×10^{-3} to 23.2×10^{-3}, with a mean of 13.52×10^{-3}. Such high ipAMS mean susceptibility (k_m) further corroborates the occurrence of low-Ti titanomagnetite as the major contributor to the ipAMS fabric (D.H. Tarling & F. Hrouda 1993). Whereas for opAMS, k_m is one or two orders lower, ranging between 4.43×10^{-5} and 1.70×10^{-4} with a mean of 9.09×10^{-5}. The low out-of-phase susceptibility perhaps reflects titanomagnetite with high-Ti content (F. Hrouda *et al.* 2022). The opAMS degree of anisotropy (i.e. *P*j ranging between 1.030 and 1.154 with a mean at 1.089) is slightly higher than that of ipAMS (*P*j ranging between 1.003 and 1.036 with a mean at 1.016). However, such a range of *P*j values, akin to other studies related to mafic dikes (e.g. C.J. Archanjo & P. Launeau 2004; W.W. Hastie *et al.* 2011; A. Das *et al.* 2021; G. Shukla *et al.* 2024, etc.), is coherent with the primary fabric originated from magma emplacement (F. Hrouda 1982). The opAMS is significantly dominated by negative shape parameter (i.e. $T < 0$), while the ipAMS shape parameter T demonstrates both positive and negative T (Fig. 5; Table 2). However, it is to be noted that the AMS parameters, such as k_m, T, P_j, do not demonstrate any gradual change as far as the spatial relationship of the samples to the dike margin is concerned.

Following C. Kissel *et al.* (2010), the AMS fabric can be classified into (a) mixed fabric consisting of distinct clusters of k_1 and k_3 axes, and (b) homogeneous/non-mixed fabric consisting of a single cluster of k_1 axis. The mixed ipAMS fabrics are observed at the eastern margin at SM2 and SM5, the dike centre at SM3, and the western margin at SM1 and SM5. The non-mixed fabrics are recorded from the eastern margin at SM4 and the western margin at SM3 and SM4. The observed mixed fabric can be resolved into subfabrics based on a distinct cluster of k_1 and k_3 axes. The ipAMS subfabrics with higher mean susceptibility are termed as subfabric A, while the subfabrics with lower mean susceptibility are termed as subfabric B. The opAMS susceptibility axes are significantly better clustered compared to ipAMS in all of the locations except for SM6. To better describe the observed fabric and subfabrics, both the ipAMS and opAMS fabrics and subfabrics were geometrically categorized into three categories (e.g. Type-I/normal fabric, anomalous fabric which is further subdivided into type-II/intermediate and type-III/inverse fabric, and type-IV/disorganized fabric) depending on the orientation of the principal susceptibility axes with respect to the dike plane based on the framework proposed by P. Rochette *et al.* (1992) and presented in Table 3. In all the cases, angular deviation of a maximum of 35° between the magnetic foliation plane (i.e. k_1–k_2) and the dike plane is considered as imbrication according to R. Shajahan *et al.* (2024).

4.2.2 AARM analyses

For robust comparison with the ipAMS and opAMS fabric, the AARM fabric types are classified into three types (i.e. normal, intermediate and inverse) following the AMS categorization framework based on the orientation of the principal axes (M_1, M_2 and M_3 i.e. maximum, intermediate and minimum, respectively) of the AARM ellipsoid (Fig. 5 and Table 3). Most of the AARM fabrics are of a different type than the ipAMS owing to reorientation of either two or all the axes. In the majority of the samples, the opAMS and AARM axes are roughly overlapping and are of a similar category (i.e. type-I/normal type). Unlike ipAMS, normal fabrics are more abundant both in AARM and opAMS fabrics. The k_1, k_2 and k_3 axes of the anomalous ipAMS fabric are replaced by the M_2, M_3 and M_1 axes in most of the normal AARM fabric. However, intermediate types of AARM fabrics are observed from the western margin at SM1, the eastern margin at SM6 and from the dike centre at SM3.

4.3. Petrography and image analysis

As evident from Fig. 6, the studied samples from the Salma dike exhibit an inequigranular texture with moderate to coarse grain size. Large phenocrysts made up of plagioclase are embedded in groundmass, that is, dominantly composed of plagioclase and clinopyroxene, showing ophitic and sub-ophitic texture (Fig. 6a). Observed inequigranular texture signifies a difference in cooling rate during different stages of the dike emplacement. The interstitial spaces of the silicate minerals are occupied by opaque minerals, which are basically Fe-Ti oxide (Figs 6a and b). Partially altered plagioclase grains are observed in samples from the central part of the dike, which implies subsolidus alteration, possibly at the late stage of the magma emplacement within the dike. Opaque minerals are observed within such altered plagioclase (Fig. 6c). Furthermore, smaller opaques are also frequently observed within the altered clinopyroxene grains at the central part of the dike (Figs 6d and e). Titanomagnetite is the dominant opaque mineral. Reflected light photomicrographs show that the titanomagnetite grains with significant exsolution and a vermicular form of the titanium-rich portion (Figs 6f and g) are at the dike centre. Besides, a minor amount of pyrite is also observed (Fig. 6g). Similar grains of exsolved titanomagnetites are also observed at the marginal part of the dike (Figs 6h and i). However, occurrences of such exsolved titanomagnetite grains are less frequent at the dike margin compared to the dike centre.

Figs 7(a) and (b) show the zoomed-out portions of the SEM photomicrographs from the dike margin. The titanomagnetite grains occupy the interstitial spaces of plagioclase and clinopyroxene groundmass, and mostly along the edges of the plagioclase grains. The titanomagnetite is mostly homogeneous along the dike margin (Fig. 7c). Smaller low-Ti (i.e. 1.1 wt per cent) titanomagnetite, compared to the larger Ti-rich (i.e. 23 wt per cent) titanomagnetite, is observed inside larger clinopyroxene (Fig. 7c) along the dike margin. In the central part of the dike, large grains of titanomagnetite are observed with a larger Ti-rich (i.e. 21.5 wt per cent) portion and a smaller Ti-poor (i.e. 8.6 wt per cent) titanomagnetite (Fig. 7d), indicating intense exsolution of primary titanomagnetite.

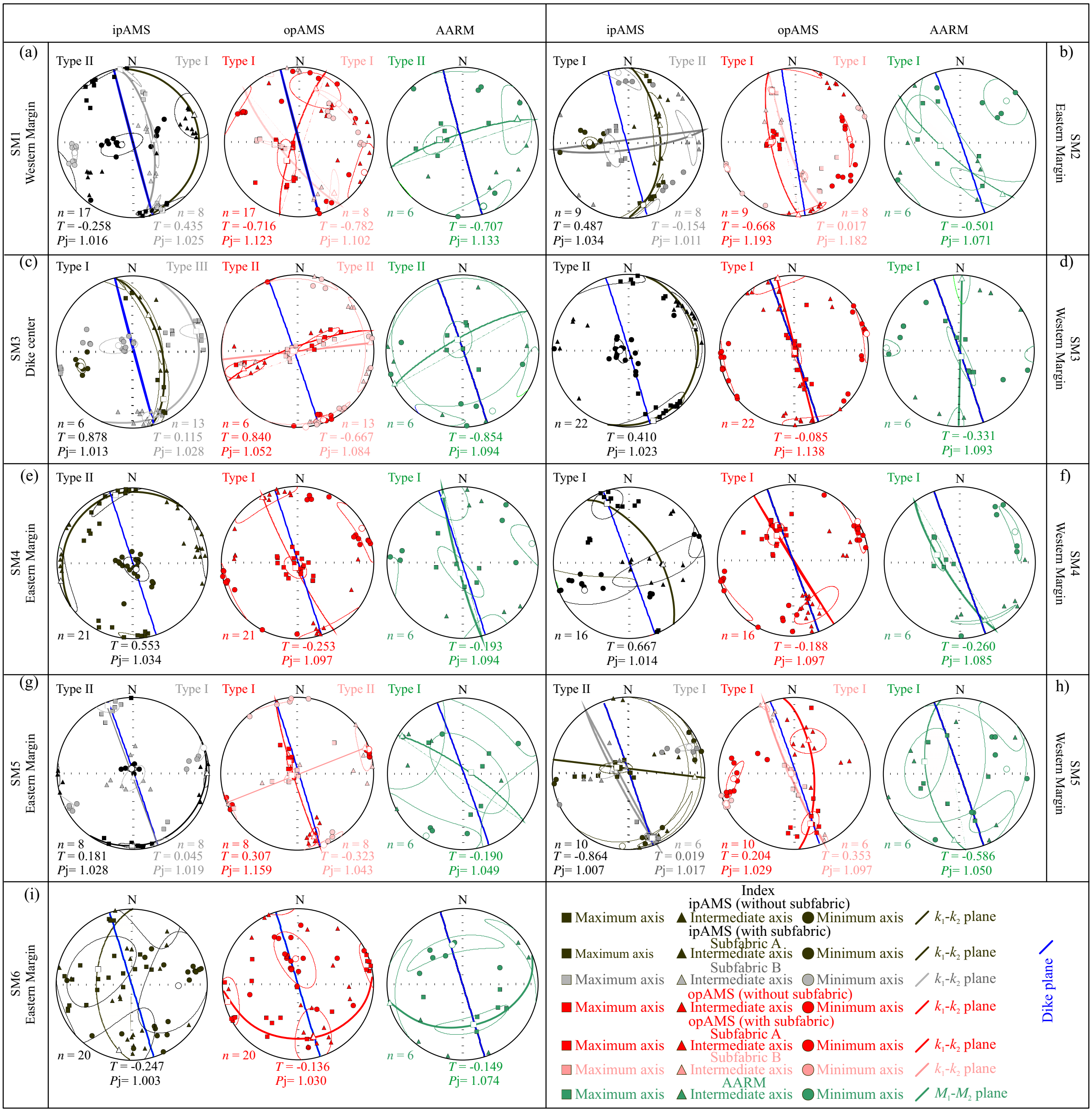

Figure 5. Stereonet plots of principal susceptibility axes of ipAMS, opAMS, and AARM fabrics. The notations and colour coding are included in the figure index. The data for individual samples are shown in Figs S5 and S6 in Section 4 of the attached Supplementary Material.

The long-axis trend distributions of the plagioclase laths are compared with the k_1–k_2 planes of the ipAMS and opAMS fabric in Fig. 8. The rose diagrams from the marginal samples depict a prominent primary maximum along or at a low angle to the dike plane. The k_1–k_2 planes of the normal ipAMS subfabric and opAMS fabric show good consistency with the primary maxima. The AARM fabric also roughly follows the primary maxima at most sites, except for the western margin at SM1 and the dike centre at SM3. At the dike centre, the plagioclase grains are rather randomly oriented and do not clearly demonstrate any particular preferred direction.

5. DISCUSSION

The combination of detailed rock-magnetic methods (i.e. k–T, field and frequency-dependent susceptibility, three-component thermal demagnetization of IRM, component unmixing modelling of IRM acquisition curve, hysteresis and FORC), microscopic observation, and joint analysis of ipAMS, opAMS and AARM sheds light on the potential origin of the observed anomalous (intermediate/inverse) fabrics. First, we evaluate the carrier for ipAMS, opAMS and AARM fabrics in terms of magnetic mineralogy. Successively, we discuss the possible sources of the observed subfabrics and the implications for magma flow direction.

Table 2. Anisotropy of magnetic susceptibility (AMS) data from different sample locations. The AMS data are graphically represented in a stereonet in Fig. 5. Specimen-wise data are shown in Tables S1 and S2 attached in Section 4 of the Supplementary Material. The graphical presentation of the ipAMS and opAMS data of the individual samples and their spatial distance from the dike margin are shown in Figs S5 and S6, respectively, in Section 4 of the Supplementary File. k_{fd} per cent = percentage of frequency-dependent susceptibility; n = Specimen No; k_m = Mean susceptibility, k_1 = Maximum susceptibility; k_2 = Intermediate susceptibility; k_3 = Minimum susceptibility; T = Shape parameter; P_j = Degree of anisotropy; D = Declination; I = Inclination.

Location	Site	k_{fd} per cent	n	Subfabric	ipAMS k_m	ipAMS P_j	ipAMS T	ipAMS k_1 D	ipAMS k_1 I	ipAMS K_2 D	ipAMS K_2 I	ipAMS K_3 D	ipAMS K_3 I	Fabric [Normal (N)/ Anomalous (A)]	Flow direction?	opAMS k_m	opAMS P_j	opAMS T	opAMS k_1 D	opAMS k_1 I	opAMS k_2 D	opAMS k_2 I	opAMS k_3 D	opAMS k_3 I	Fabric [Normal (N)/ Anomalous (A)]	Flow direction?
SM1	SM1 Western	0.85	17	A	13.47E-3	1.016	-0.258	156	2	66	12	258	77	A	Discarded	4.96E-05	1.123	-0.716	214	65	23	24	115	4	N	Subvertical
(23°47′23.46″N;	margin		8	B	8.341E-03	1.025	0.435	350	2	86	67	259	22	N	Subvertical	4.21E-05	1.102	-0.782	264	56	145	17	46	27	N	Subvertical
86°57′24.00″E)																										
SM2	SM2 Eastern	0.96	9	A	14.34E-03	1.034	0.487	167	11	67	40	270	46	N	Subvertical	7.62E-05	1.193	-0.668	266	62	172	2	81	27	N	Subvertical
(23°44′26.34″N;	margin		8	B	9.907E-03	1.011	-0.154	244	70	83	18	351	6	A	Discarded	9.58E-05	1.182	0.017	339	26	155	63	248	1	N	Subvertical
86°58′34.99″E)																										
SM3	SM3 Centre	0.91	6	A	13.12E-03	1.013	0.878	147	26	24	46	254	30	N	Discarded[a]	9.90E-05	1.052	0.840	61	50	251	38	157	4	A	Discarded
(23°43′44.10″N;			13	B	12.90E-03	1.026	0.115	72	12	164	10	294	73	A	Discarded	1.10E-04	1.080	-0.667	269	85	85	4	175	0	A	Discarded
86°58′49.67″E)	SM3 Western margin	1.18	22	–	16.17E-03	1.023	0.410	160	2	70	8	268	81	A	Discarded	1.02E-04	1.138	-0.085	127	87	343	2	253	1	N	Subvertical
SM4	SM4 Eastern	0.80	21	–	16.59E-03	1.034	0.553	349	5	259	3	137	83	A	Discarded	1.04E-04	1.097	-0.253	202	84	331	3	61	4	N	Subvertical
(23°39′37.56″N;	margin																									
87° 0′31.08″E)	SM4 Western margin	0.77	16	–	6.619E-03	1.014	0.667	339	17	93	52	238	31	N	Subvertical	4.52E-05	1.097	-0.188	329	52	151	37	60	1	N	Subvertical
SM5	SM5 Eastern	1.14	8	A	25.97E-03	1.028	0.181	180	5	90	1	343	84	A	Discarded	2.23E-04	1.159	0.307	336	76	161	13	71	1	N	Subvertical
(23°37′50.23″N;	margin		8	B	20.51E-03	1.019	0.045	339	5	174	84	70	1	N	Discarded[b]	1.17E-04	1.043	-0.323	241	83	78	6	347	2	A	Discarded
87° 1′18.22″E)	SM5 Western	1.24	10	A	12.31E-03	1.007	-0.864	292	75	93	14	185	4	A	Discarded	1.17E-04	1.029	0.204	162	31	23	51	265	20	N	Subvertical
	margin		6	B	10.96E-03	1.017	0.019	159	9	282	72	67	14	N	Subvertical	9.49E-05	1.097	0.353	95	86	335	1	245	2	N	Subvertical
SM6	SM6 Eastern margin	1.13	20	–	10.39E-03	1.003	-0.247	295	49	190	12	91	37	Disorganized	Discarded	4.43E-05	1.030	-0.136	256	4	163	27	354	62	Disorganized	Discarded

[a]The combination of normal ipAMS, anomalous opAMS, anomalous AARM, and the presence of some amount of SD grains at the dike centre suggests a preferred orientation of magnetic minerals contributing to this fabric at a high angle to the dike plane (F. Hrouda *et al.* 2020). At the dike centre, the plagioclase laths are randomly oriented (Fig. 7). So, the magnetic minerals occurring at the interstitial spaces might not be related to the flow. Rather, the observed fabric may be related to the post-emplacement processes (e.g., back-flow of magma, reworking and subsequent collapse of the 3-D plagioclase framework). Intense late-stage alteration is observed at the dike centre. Therefore, despite being a normal fabric, it is discarded.

[b]The combination of normal ipAMS, anomalous opAMS, anomalous AARM and SD grains suggests a preferred orientation of magnetic minerals contributing to this fabric at a high angle to the dike plane (F. Hrouda *et al.* 2020). Therefore, despite being a normal fabric, subfabric B at the eastern margin of SM5 is discarded.

Table 3. Geometric categorization of magnetic fabric and subfabrics; k_m = Mean susceptibility, T = Shape parameter; P_j = Degree of anisotropy

Fabric type		Homogeneous fabric ipAMS	Homogeneous fabric opAMS	Mixed fabric ipAMS Subfabric A	Mixed fabric ipAMS Subfabric B	Mixed fabric opAMS Subfabric A	Mixed fabric opAMS Subfabric B	AARM
Type-I/Normal: k_1–k_2 plane parallel or at a low angle to the dike plane		***Western margin***: SM4 (k_m = 6.619E-03; T = 0.667; P_j = 1.014; Fig. 5f)	***Western margin:*** a) SM3 (k_m = 1.02E-04; T=-0.085; P_j = 1.138; Fig. 5d) b) SM4 (k_m = 1.04E-04; T=-0.253; P_j = 1.097; Fig. 5f)	***Eastern margin:*** SM2 (k_m = 14.34E-03; T = 0.487; P_j = 1.034; Fig. 5b) ***Dike centre:*** SM3 (k_m = 13.12E-03; T = 0.878; P_j = 1.013; Fig. 5c)	***Western margin:*** a) SM1 (k_m = 8.341E-03; T = 0.435; P_j = 1.025; Fig. 5a), b) SM5 (k_m = 10.96E-03; T = 0.019; P_j = 1.017; Fig. 5h) ***Eastern margin:*** SM5 (k_m = 20.51E-03; T = 0.045; P_j = 1.019; Fig. 5g)	***Western margin:*** a) SM1 (k_m = 4.96E-05; T = -0.716; P_j = 1.123; Fig. 5a) b) SM5 (k_m = 1.17E-04; T=-0.204; P_j = 1.029; Fig. 5h) ***Eastern margin:*** a) SM2 (k_m = 7.62E-05; T=-0.668; P_j = 1.193; Fig. 5b) b) SM5 (k_m = 2.23E-04; T = 0.307; P_j = 1.159; Fig. 5g)	***Western margin:*** a) SM1 (k_m = 4.21E-05; T = -0.782; P_j = 1.102; Fig. 5a) b) SM5 (k_m = 9.49E-05; T = 0.353; P_j = 1.097; Fig. 5h) ***Eastern margin:*** SM2 (k_m = 9.58E-05; T = 0.017; P_j = 1.082; Fig. 5b)	***Eastern Margin:*** a) SM2 (T=-0.501; P_j = 1.071; Fig. 5b) b) SM4 (T = -0.193; P_j = 1.094; Fig. 5e) c) SM5 (T = -0.190; P_j = 1.049; Fig. 5g) ***Western margin:*** a) SM3 (T=-0.331; P_j = 1.093; Fig. 5d) b) SM4 (T = −0.260; P_j = 1.085; Fig. 5f) c) SM5 (T = −0.586; P_j = 1.050; Fig. 5h)
Anomalous fabric	***Type-II/Intermediate:*** k_1–k_3 along the dike plane	***Western margin:*** SM3 (k_m = 16.17E-03; T = 0.410; P_j = 1.023; Fig. 5d) ***Eastern margin***: SM4 (k_m = 16.59E-03; T = 0.553; P_j = 1.034; Fig. 5e)		***Western margin:*** a) SM1 (k_m = 13.47E-3; T=-0.258; P_j = 1.016; Fig. 5a) b) SM5 (k_m = 12.31E-3; T = -0.864; P_j = 1.007; Fig. 5h) ***Eastern margin:*** SM5 (k_m = 25.97E-03; T = 0.181; P_j = 1.028; Fig. 5g)	***Eastern margin:*** SM2 (k_m = 9.907E-3; T=-0.154; P_j = 1.011; Fig. 5b)	***Dike centre:*** SM3 (k_m = 9.90E-05; T = 0.840; P_j = 1.052; Fig. 5c)	***Eastern margin:*** SM5 (k_m = 1.17E-04; T = -0.323; P_j = 1.043; Fig. 5g) ***Dike centre:*** SM3 (k_m = 1.10E-04; T = -0.667; P_j = 1.084; Fig. 5c)	***Western margin:*** SM1 (T = -0.707; P_j = 1.133; Fig. 5a) ***Dike centre:*** SM3 (T = -0.854; P_j = 1.094; Fig. 5c) ***Eastern margin:*** SM6 (T = -0.149; P_j = 1.074; Fig. 5c)
	Type-IIII/Inverse: k_2–k_3 along the dike plane				***Dike centre:*** SM3 (k_m = 12.90E-03; T = −0.115; P_j = 1.028; Fig. 5c)			
Type-IVDisorganized/Scattered fabric				Only at the eastern margin at SM 6 (Fig. 5i)				

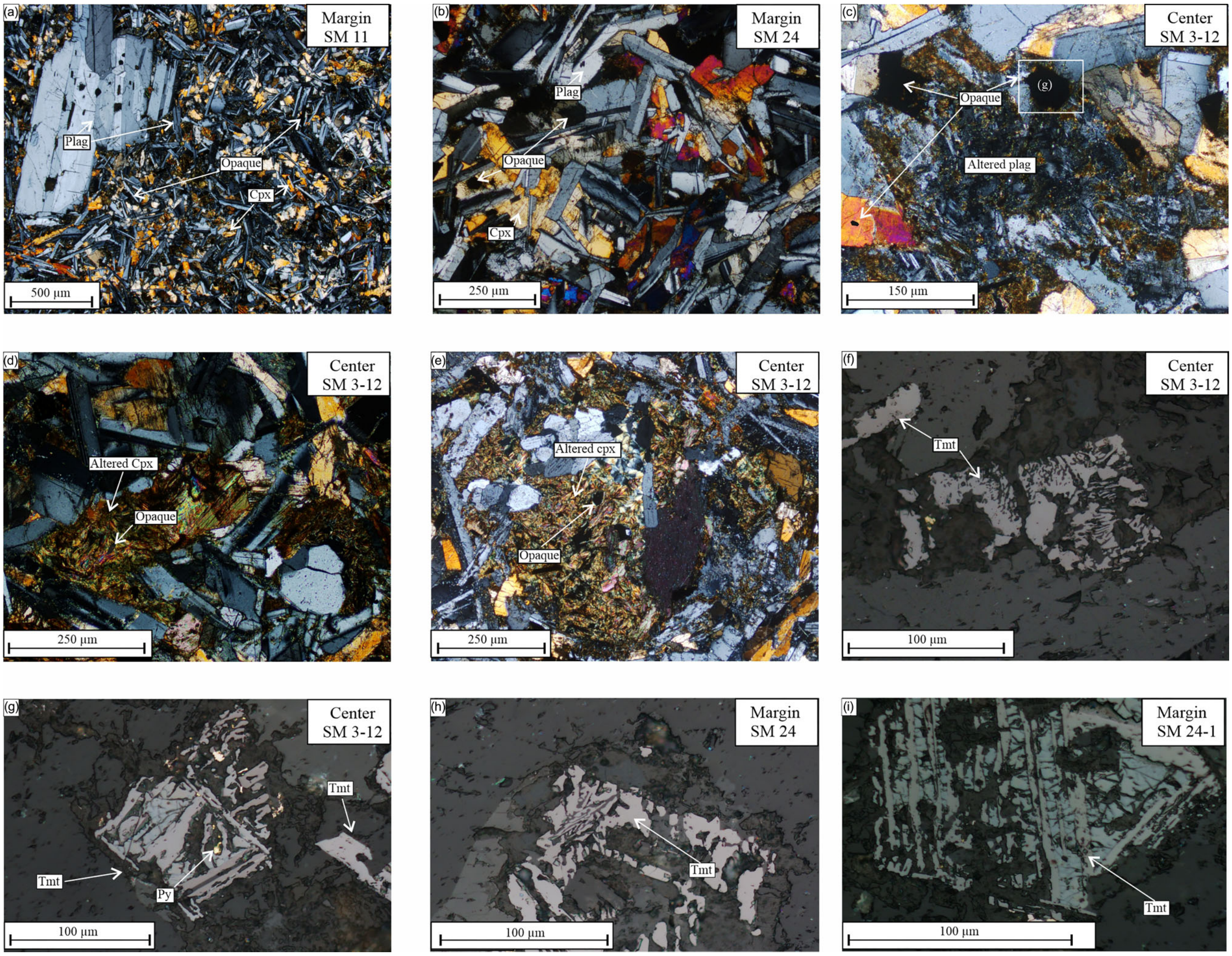

Figure 6. (a)–(e) Transmitted light photomicrographs of Salma dike samples showing plagioclase phenocrysts embedded in groundmass governed by silicate minerals like plagioclase and clinopyroxene. Opaque minerals (Fe-Ti oxides) occupy the interstitial spaces of Silicate minerals. In the central part of the dike, alteration of silicate grains (Clinopyroxene and plagioclase) is evident. (f)–(i) Reflected light photomicrographs showing titanomagnetite grains with Ti-rich and Ti-poor admixtures. It is to be noted that titanomagnetite grains are intensely exsolved into Ti-rich and Ti-poor admixtures at the dike centre. Along the dike margin, such exsolved admixtures are observed less frequently. Rather, homogeneous grains are more common along the margin. Plag: plagioclase; Cpx: Clinopyroxene; tmt: titanomagnetite.

5.1. Mineralogical source of the observed magnetic (ipAMS, opAMS and AARM) fabric

The absence of a Verwey transition in the low-temperature k–T curve suggests no stoichiometric pure magnetite (Figs 2a–d). The high-temperature k–T curves, with Curie temperature above 550°C, suggest a phase with composition close to stoichiometric magnetite with very low-Ti content is present in the samples (Fig. 2). Additional Curie temperature at ∼ 470°C and ∼ 300°C also suggests titanomagnetite with moderate Ti content (Figs 2a–d). The presence of titanomagnetite with variable Ti content is also evident in the petrographic study, SEM-EDS observations and thermal demagnetization of the three-axis IRM. The component unmixing of the IRM curves further confirms the presence of at least two components with varying compositions or/and grain-size (Figs 3f–j). The weak field-dependence of ipMS (k_{Hd} per cent $<$ 1 per cent for the majority of the samples; Fig. 2e) implies that low-Ti titanomagnetite governs the ipMS and, in turn, the observed ipAMS fabric. Whereas, the opMS demonstrates observable variation (i.e. k_{Hd} per cent ranging between 20 and 50 per cent) with the field (Fig. 2f), suggesting that higher Ti titanomagnetite is responsible for the observed opMS signal and consequently the opAMS fabric (F. Hrouda *et al.* 2019). The AARM fabrics are governed by all the ferromagnetic grains present in the samples. However, since the AARM and opAMS axes are overlapping for most samples, the AARM signal might be less sensitive or even insensitive to pure magnetite grains (except for very small grains), whose phase angle and the opMS are effectively zero (F. Hrouda *et al.* 2017).

5.2. Origin of the anomalous (intermediate/inverse) fabric

The presence of subfabrics, along with the deviation of the ipAMS fabrics from the opAMS and AARM fabrics in the majority of the sites, suggests that the fabrics are composite and were probably associated with either magnetic mineralogy or different magmatic processes related to emplacement. The composite or mixed fabrics could be caused by intense metasomatic processes (P.F. Silva *et al.* 2008) or by minerals crystallized at different stages of magma emplacement (P.F. Silva *et al.* 2014).

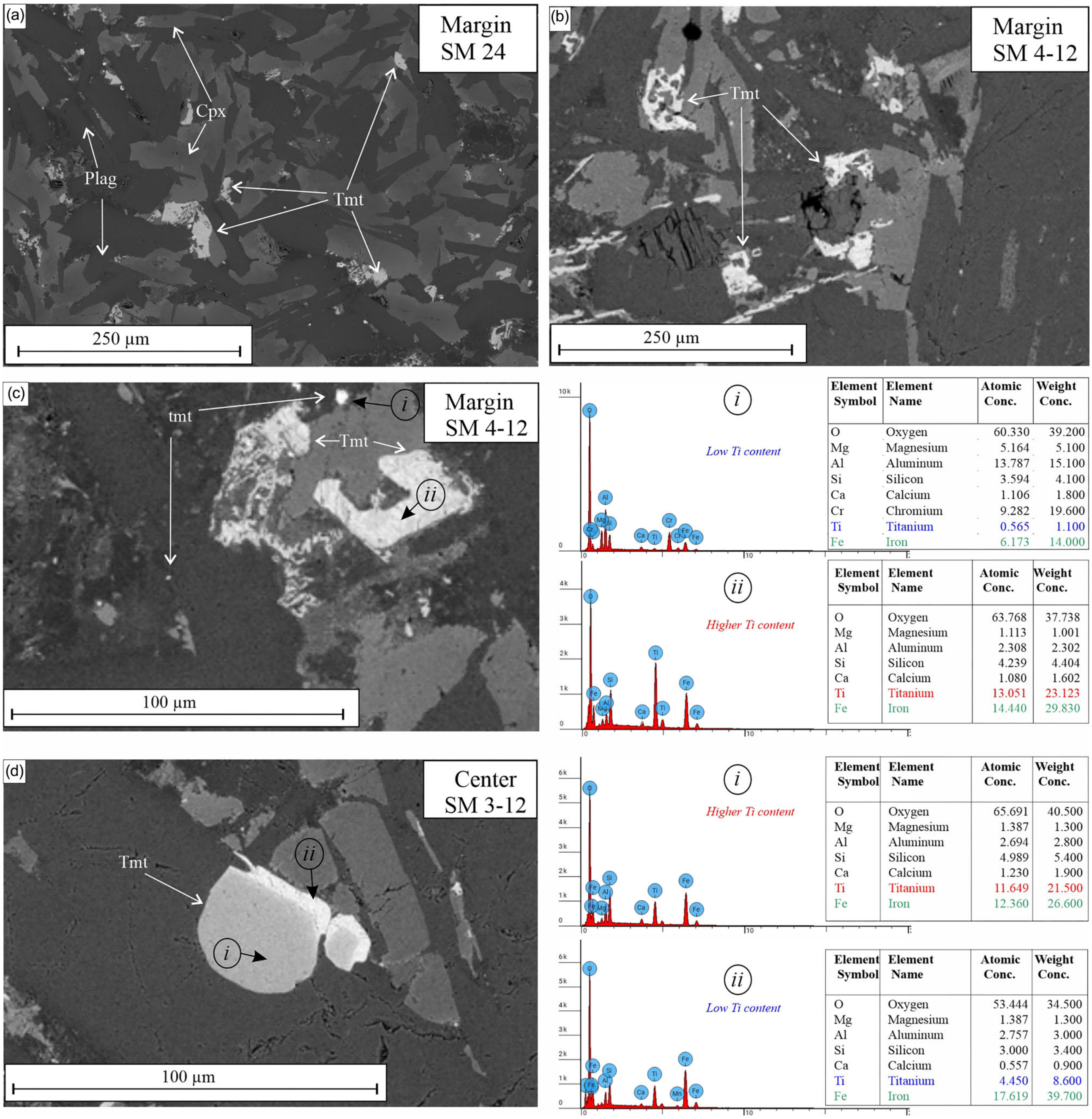

Figure 7. (a)–(b) SEM images showing the occurrence of titanomagnetite along the silicate minerals in the samples from the dike margin. (c) SEM images of the samples from the dike margin showing homogeneous grains of titanomagnetite with higher Ti content in the silicate groundmass and smaller grains of low-Ti titanomagnetite inside large clinopyroxene grains. EDS data of the marked points (e.g. i and ii) are presented in the right panel. (d) SEM image of a sample from the dike centre exhibiting intense oxyexsolution of Fe-Ti oxide into larger Ti-rich titanomagnetite and smaller lower Ti titanomagnetite parts. EDS data of the marked points (e.g. i and ii) are presented in the right panel. All the abbreviations are similar to Fig. 6

Moreover, composite fabrics are often associated with exsolution of Fe-Ti oxides, promoting SD dominance (P.F. Silva *et al.* 2008). F. Hrouda *et al.* (2020) showed that in the case of normal preferred orientation of the titanomagnetite grains with the longer dimension along the dike plane, where SD grains dominate, the opAMS and AARM fabric would be normal, and the ipAMS fabric would be intermediate/inverse. Keeping this in mind, the majority of the intermediate ipAMS fabric and subfabrics are associated with corresponding normal opAMS and AARM fabric along the dike margin (Fig. 5; Table 3), suggesting the dominance of SD grains at the majority of the sites. Most of the data points follow the SD–MD trend for magnetite on the Day-Dunlop plot, which is valid for the ipAMS fabric as it is sourced from very low-Ti titanomagnetite. According to A.P. Roberts *et al.* (2000), a mixture of SD and MD grains can result in an average PSD-like signature. However, our FORC analyses suggest dominance of PSD grains with varying influence of SD grains for all the studied samples except for SM21. The SD tail in the FORC analyses certainly portrays the influence of smaller SD grains all along the dike margin. However, the

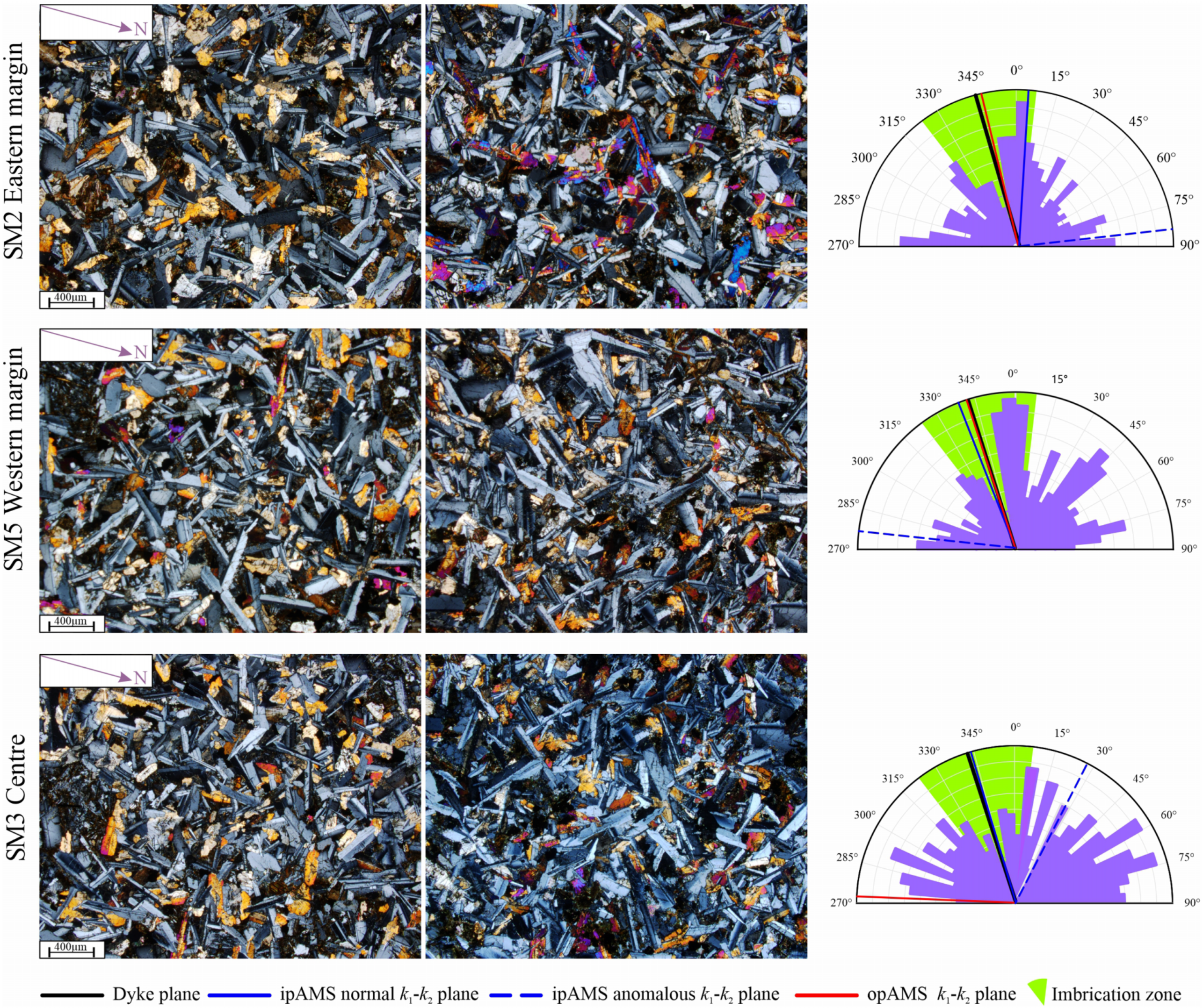

Figure 8. Image analysis on two thin sections from the dike margin at site SM2 and SM5 and one thin section from the dike centre. Thin sections have been cut along the dike plane containing the k_1–k_2 plane of normal opAMS fabric, normal ipAMS subfabric in the marginal sample. The Rose diagrams show the long-axis trend distribution of plagioclase obtained with the software program ImageJ (W.S. Rasband 2012) and Georose software. Within the rose diagrams, we plotted the orientation k_1–k_2 plane of the normal ipAMS subfabric and opAMS fabric.

SEM-EDS analyses (e.g. Fig. 7c) reveal smaller grains of low-Ti titanomagnetite as inclusions within larger clinopyroxenes along the dike margin. These observations are consistent with the small low-Ti titanomagnetite grains that may have crystallized from the interstitial melt after the flow froze rapidly at the marginal part (S.A. Martin *et al.* 2019). However, the contribution of subsolidus exsolution or secondary alteration cannot be excluded. Moreover, exsolved grains of titanomagnetite are also observed along the dike margin (Fig. 6i), albeit much less frequently than the dike centre, suggesting high-temperature exsolution of the primary titanomagnetite (P.F. Silva *et al.* 2008). Therefore, the observed intermediate ipAMS fabric and subfabrics along the margin could be a combined effect of such late-stage cooling (S.A. Martin *et al.* 2019), rare high-temperature exsolution (P.F. Silva *et al.* 2008), and SD effect depicted by the FORC diagram (F. Hrouda *et al.* 2020). The opAMS can be produced by very fine grains at the superparamagnetic and stable SD threshold (i.e. SP/SD), but not by stable SD grains (F. Hrouda *et al.* 2020). Our FORC and frequency-dependent susceptibility data show almost no or negligible SP content. Therefore, the coarser (PSD or MD) fraction of titanomagnetite grains observed along the plagioclase and clinopyroxene grains under the microscope is the main contributor to the opAMS. Moreover, it is to be noted that the AARM fabrics need not be similar to the opAMS fabric in rocks consisting of more than one component of ferromagnetic minerals if the governing ferromagnetic subfractions are different in terms of composition as well as orientation (F. Hrouda *et al.* 2020). Such a scenario is observed at the western margin of SM1, where the AARM fabric is intermediate, unlike the normal opAMS fabric, and supported by the evidence of at least two components of titanomagnetite with varying Ti content from rock-magnetic analyses (Figs 2, 3) and SEM-EDS (Fig. 7).

At the dike centre of SM3, ipAMS subfabric B is inverse. Whereas both the opAMS and AARM fabrics are geometrically intermediate. Such fabrics cannot be explained simply with the SD effect, even though an SD tail is evident on the FORC diagram. The ipAMS subfabric A shows a normal configuration, unlike the other fabrics in the central part of SM3. According to F. Hrouda *et al.* (2020), a combination of normal ipAMS along with an anomalous opAMS, and AARM fabrics may represent the inverse shape preferred orientation of the SD-dominated ferromagnetic grains at a high angle to the dike plane. FORC diagrams depict the presence of SD grains both at the dike centre (SM3; Fig. 4f) and the eastern margin (SM5; Fig. 4i). The late-stage alterations of silicate grains, such as clinopyroxene and plagioclase, and Fe-Ti oxides with intense Ti-rich and Ti-poor admixtures are frequently observed at the dike centre, which may be a consequence of metasomatism due to a prolonged period of cooling (P.F. Silva *et al.* 2008). Larger composite grains of titanomagnetite (with Ti-rich and Ti-poor admixture) prevail at the dike centre, unlike the marginal part, where comparatively smaller homogeneous grains of Fe-Ti oxide dominate. Such observations are also compatible with the slower cooling rate at the dike centre. So, post-emplacement or late-stage alterations and intense high-temperature exsolutions of the primary titanomagnetite grains must have played a significant role in the observed anomalous fabric at the dike centre.

5.3. Do these magnetic fabrics represent a flow fabric?

The preferred orientation of the plagioclase laths along or at a low angle to the dike plane indicates the primary flow direction. D. Trippanerra *et al.* (2020) reported randomly oriented plagioclase laths in the margins of dikes from eastern Iceland. They suggested it was due to interference from fracture networks developed during different stages of dike cooling. In such a scenario, they cautioned against interpreting the fabric in terms of primary flow direction. We did not observe such fractures or cooling joints in the field. Moreover, in the case of the Salma dike, the primary maxima of the long-axis trend distribution of the plagioclase laths are at a low angle to the dike plane at the margins, thereby representing flow direction (Fig. 8). The magnetic foliation planes of the normal ipAMS, opAMS and AARM fabrics roughly follow the long-axis trend of plagioclase laths along the dike plane, and represent the flow fabric, unlike the anomalous (intermediate/inverse) fabrics and subfabrics. However, a secondary maximum is noted in the samples from the dike margin by a group of plagioclase grains. These secondary maxima can, perhaps, explain the combination of normal ipAMS subfabric B with anomalous opAMS subfabric at the eastern margin at SM5, which, according to F. Hrouda *et al.* (2020), is an indication of anomalous shape preferred orientation at high angle to the dike plane. In this case, the k_1–k_2 planes of the intermediate opAMS subfabric B oriented along the minor secondary maxima imply a combined effect of the plagioclase framework, along with the late-stage cooling and alteration processes. So, these fabrics at the eastern margin of SM5 do not represent the flow fabric. Such secondary maxima can result from partial melt-back of the chilled margin by the outward heat flux from the magma flowing in the dike interior (H.E. Huppert & R.S.J. Sparks 1989; S.A. Martin *et al.* 2019). Due to rapid cooling at the dike margin, viscosity increases. As a combined effect of progressive hardening of the dike margin and shearing due to flowing magma at the dike interior, the quasi-viscous mixture of melt and crystal (possibly caused by the melt-back mechanism) could have led to the grain orientation at a high angle to the dike plane (B.K. Holtzman *et al.* 2005; P.F. Silva *et al.* 2014). However, such a melt-back mechanism was not significant enough to melt the entire chilled margin. Consequently, conduction-driven rapid cooling at the dike margin against the host rock during emplacement facilitated the preservation of primary magma flow direction as indicated by the observed primary maxima of the plagioclase laths and the normal magnetic fabrics. At the dike centre of SM3, the long-axis trend distribution of plagioclase is scattered, which is likely at the central part of the thick dike due to back-flow of magma and convection after the flow has stopped (A. Das & J. Mallik 2020). Furthermore, the huge thickness (i.e. >70 m) of the studied Salma dike suggests that reworking and subsequent collapse of the 3-D plagioclase framework is a distinct possibility (A.R. Philpotts & L.D. Dickson 2000). Therefore, the magnetic fabric observed at the dike centre is not related to flow. The fabrics observed at the eastern margin of SM6 are disorganized and highly scattered. Such fabrics are documented in almost all the studies and lack any clear explanation other than a complex and turbulent flow pattern (C. Kissel *et al.* 2010). Therefore, such fabrics are excluded from further interpretation.

5.4 Determination of magma flow direction and its implications

Considering the above discussion about the magnetic fabric in terms of magma flow, the magma flow direction is determined only from the normal ipAMS, opAMS, and AARM fabric along the dike margin. To calculate the flow direction, the imbrication of magnetic foliation planes and magnetic lineation was considered for $T > 0$ and $T < 0$, respectively (L. Geoffroy *et al.* 2002; J.-P. Callot & L. Geoffroy 2004; A. Delcamp *et al.* 2015). The dike is dominated by subvertical flow (Fig. 9). Such dominance of subvertical flow could have been caused by dike offsets (A. Gudmundson 1990; R. Ray *et al.* 2007). However, we did not observe any macro/mesoscale offset segments in the field. Therefore, assuming that there was no shear movement of the dike wall involved, the magma fed the dike vertically from the feeder source. At this stage of emplacement, magma was also subjected to advective heat loss, thereby crystallizing the minerals. In this stage, ferromagnetic minerals are likely to crystallize in the interstitial spaces of silicate grains, governing the primary flow fabric and ending up providing a subvertical flow direction. We propose that the large MD/PSD titanomagnetite and low-Ti titanomagnetite/magnetite grains, likely governing the normal ipAMS, opAMS and AARM fabrics, used the interstitial spaces of plagioclase and clinopyroxene grains as the site for nucleation and grew unhindered into large size following the silicate template (S.A. Martin *et al.* 2019). But smaller SD titanomagnetite, responsible for the majority of the intermediate fabric along the dike margin, might have formed through a complex process. The origin of such small grains, either due to late-stage crystallization from the interstitial melt or alteration of the pre-existing phases, is attributed to the limited space for unhindered growth once the flow has stopped. Furthermore, even coarser grains of Fe-Ti oxide with intense exsolution in terms of Ti-rich and Ti-poor admixtures are observed both at the dike margin and centre, which can reduce the effective grain size and promote a single domain magnetic phase (P.F. Silva *et al.* 2008). The absence of imprints related to tectonic deformation in the field and microstructural observation also suggests that such anomalous fabrics are only related

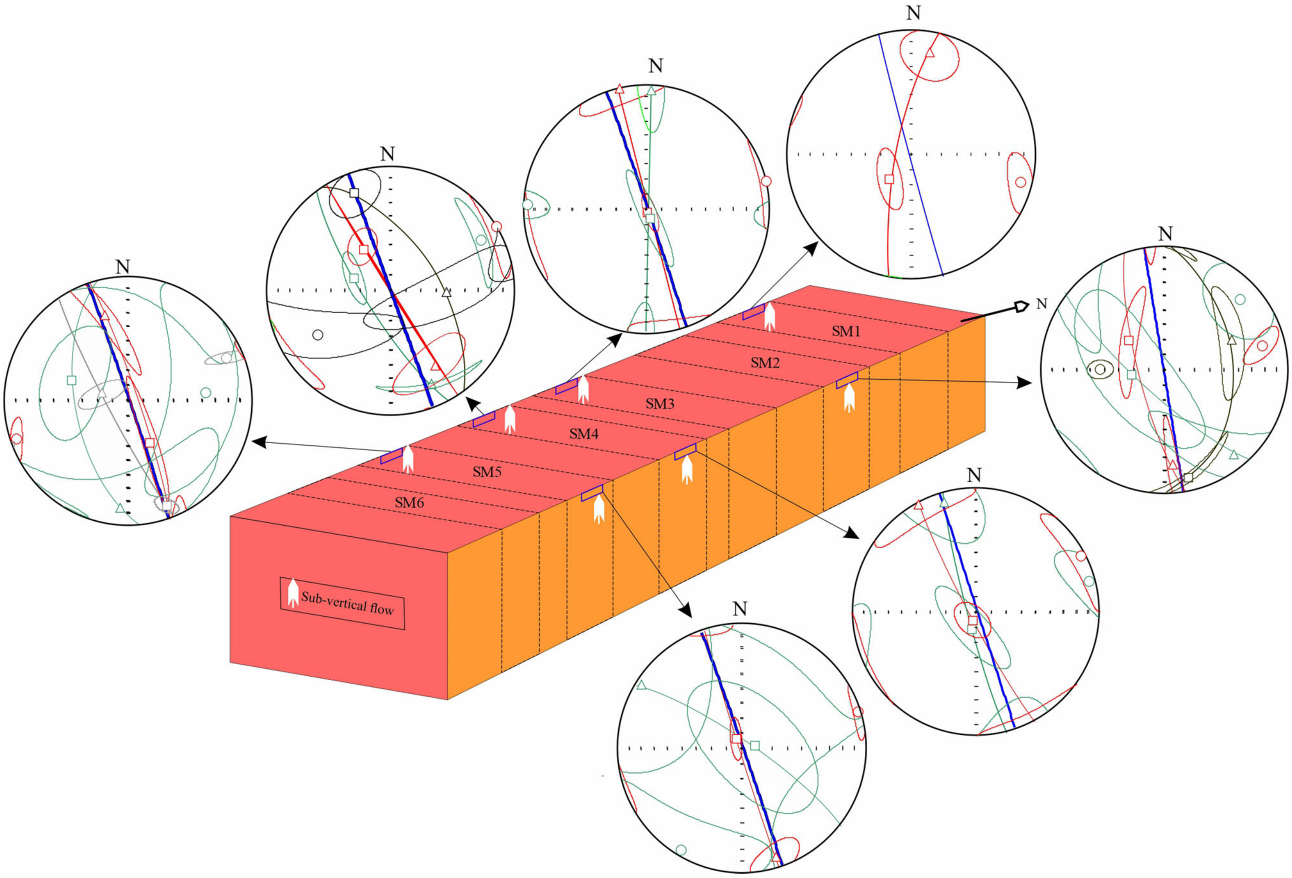

Figure 9. Inferred flow directions from normal ipAMS, opAMS and AARM are plotted on the 3-D diagram of the Salma dike. Stereonets show the possible imbrication of the magnetic foliation plane from both the dike margins. Inferred flow directions demonstrate dominance of subvertical. Colour index of the data points on the stereonets is similar to Fig. 5. The normal opAMS subfabrics of each site are combined, noting a small angular difference.

to the late-stage/post-emplacement processes. Therefore, considering the normal fabrics, we conclude that the dike was fed subvertically.

Magma flow pattern is an important parameter that reflects the ascent path of magma in the dike. Based upon the pioneering research about magma transport through dikes (R.E. Ernst & W.R.A. Baragar 1992; Y.A. Fialko & A.M. Rubin 1999; A. Das *et al.* 2021), magma is expected to inject vertically through the dikes from a magma source situated just below it and to inject more and more laterally away from the chamber. The Mackenzie dike swarm of Canada is a classic example of such a flow pattern (J.D. Greenough & J.P. Hodych 1990; R.E. Ernst & W.R.A. Baragar 1992). A. Delcamp *et al.* (2015) reported a similar scenario from the dike swarm of the Tenerife rift zone, where they postulated the vertically emplaced dikes to be located at the summit and laterally emplaced dikes at the flanks. In the context of the RT, M.R. Kapawar *et al.* (2021) studied the lava flow sequences (Fig. 1a) and inferred NE–SW trending lateral flow. Based on the trend of the magma flow direction, M.R. Kapawar *et al.* (2021) further suggested the Comei-Cona basaltic suite, located thousands of kilometres away in Tibet, to be the shallow source feeding the RT basalts. On the contrary, this study suggests that, in the case of the Salma dike, the observed magnetic fabrics show vertical magma flow at the present level of exposure, indicating that the magma ascended from depth. Although these data do not conclusively identify the deep magma source, they are consistent with a scenario in which the feeder source lies directly beneath the dike. Gravity modelling data of A.P. Singh *et al.* (2004) also detected a high-density subcrustal magmatic body beneath the region and further ascribed it to be the 'igneous crustal accretion' beneath the RT. Such crustal accretion can be explained either by thermal perturbation due to decompression melting (D.L. Anderson 2000) or by the Kerguelen plume head (W.J. Morgan 1981; R.K. Srivastava *et al.* 2023). Owing to the proximity of the Salma dike to the high-density subcrustal magmatic pond beneath the RT, it is energetically favourable for the magma to come up directly rather than travelling thousands of kilometres.

Considering all these arguments, we propose that the Salma dike could have been vertically fed from the subcrustal magma pond located beneath the RT (Fig. 10). However, a detailed comparison of the Salma dike with the RT flows, in terms of both geochemistry and paleomagnetism, is required to determine whether it served as a feeder dike to the RT. Furthermore, to better understand the emplacement mechanism as well as the associated geodynamic scenario for the entire RT, thorough investigations from other dikes located in Giridih, Koderma and Raniganj areas, as well as further studies of the RT flows, are required.

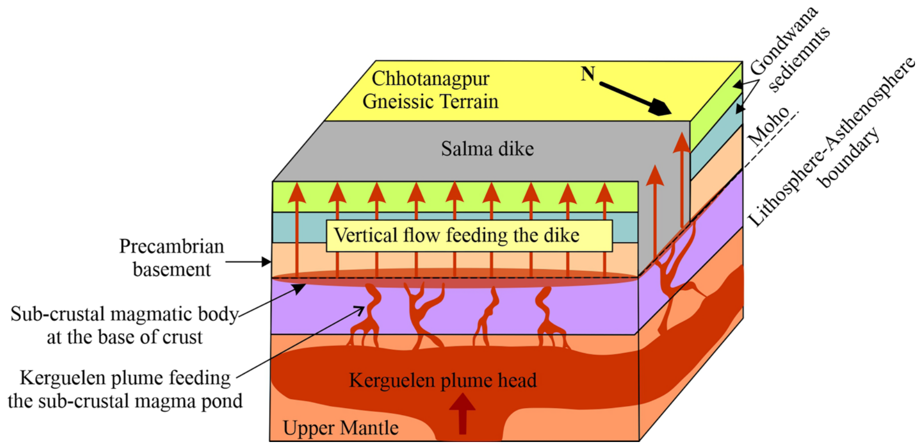

Figure 10. Hypothetical figure showing a plausible scenario explaining how the vertical flow from a subcrustal magma pond delineated by A.P. Singh *et al.* (2004) (modified after T. Mittal & M.A. Richards 2021) could have fed the dike. The Kerguelen plume supplied the heat and molten material to the subcrustal magmatic body (R.K. Srivastava *et al.* 2019a, 2023).

6. CONCLUSION

In this article, the ∼116 Ma old Salma dike is explored for the first time in terms of high-resolution rock-magnetic and magnetic fabric characteristics. A joint analysis of ipAMS, opAMS and AARM fabrics is undertaken to characterize the observed petro-fabric in the Salma dike, to envisage its magma emplacement mechanism. We characterized the magnetic fabrics in terms of their contributing phases as well as their implications in light of rock-magnetic attributes. Our findings can be summarized as follows:

(a) Rock-magnetic measurement reveals that the Salma dike contains two types of titanomagnetite with variable Ti content that fall within the PSD range, with a varying content of SD grains in the majority of the sites. The ipAMS fabric is mostly contributed by low-Ti titanomagnetite. The opAMS fabrics are governed by titanomagnetite with higher Ti content. AARM fabrics are caused by all the ferromagnetic grains present in the samples.
(b) Majority of the opAMS fabrics are of normal type, that is, k_1–k_2 plane is sub-parallel to the dike plane except for the dike centre. Whereas, the majority of the ipAMS fabrics are of an anomalous type with k_1–k_2 plane perpendicular to the dike. The majority of AARM and opAMS fabrics are coaxial in the majority of the sites except for the western margin at SM1.
(c) Comparison between ipAMS, opAMS and AARM, as well as the presence of some SD grains in the FORC analyses, suggests that these grains mostly caused the observed intermediate ipAMS fabric along the dike margin. The origin of such small grains is attributed to their growth in a tight space during late-stage crystallization from interstitial melt or post-emplacement alteration. At the dike centre, the combined effect of intense alteration of the primary silicate grains (e.g. clinopyroxene), post-emplacement magma backflow, as well as reworking and collapse of the silicate groundmass could have caused the anomalous fabric, i.e., not related to the flow.
(d) Magma flow direction derived from the normal ipAMS fabrics and subfabrics, and opAMS, AARM fabric exhibits a dominance of subvertical flow.
(e) Vertical feeding flow direction indicates magma ascent from depth beneath the RT. This inference is compatible with the plausible scenario that a high-density subcrustal magmatic layer might have acted as the feeder chamber, which could be explained either by thermal perturbation due to decompression melting or by the Kerguelen plume head.

SUPPORTING INFORMATION

Supplementary data are available at *GJIRAS* online.

Figure S1. Plots showing the variation of ipAMS (k') and opAMS (k") with grain size (ranging from SP to SD through SP/SD) of magnetite and titanomagnetite, respectively (modified after F. Hrouda *et al.* 2020).
Figure S2. A schematic diagram showing the distribution of nine sampling sites from the six selected sampling locations. It also shows the spatial interval of the samples from the dike margin.
Figure S3. Temperature-dependent susceptibility (k–T) curve for the samples which are not presented inside the paper in Fig. 2
Figure S4. Thermal demagnetization of three-Axes IRM data for all the studied samples.
Figure S5. Sample-wise in-phase AMS data according to the spatial distribution of the individual samples from the margin. EB: Eastern boundary; WB: Western Boundary; C: Centre. Data points follow the same legend according to Fig. 5 in the paper.
Figure S6. Sample-wise out-of-phase AMS data according to the spatial distribution of the individual samples from the margin. EB: Eastern boundary; WB: Western Boundary; C: Centre. Data points follow the same legend according to Fig. 5 in the paper.
Table S1. ipAMS data.
Table S2. opAMS data

ACKNOWLEDGMENTS

AD thanks the Polish National Agency for Academic Exchange (NAWA) for the Ulam NAWA scholarship (grant no. BPN/ULM/2023/1/00109/DEC/1) to conduct this research in the Institute of Geophysics Polish Academy of Sciences (IGF PAN), Warsaw, Poland. The authors thank the Institute of

Geophysics Polish Academy of Sciences, for financial support for fieldwork and sample transportation. The authors thank Mr Sutanu Das for his assistance during fieldwork in India. The authors also thank Dr Tomasz Werner for his help during laboratory operations. The authors thank Dr Michael S. Petronis, Dr Bjarne Almqvist and another anonymous reviewer for their insightful and valuable review of the manuscript. The authors also extend their gratitude to the editor, Dr Eduard Petrovsky, for his valuable feedback to improve the manuscript.

DATA AVAILABILITY

The data underlying this article are available in the article and in the supplementary material. The supplementary file is divided into four sections (Sections 1–4). Section 1 contains the theory of in-phase and out-of-phase AMS, Section 2 contains the schematic diagram of sampling location and sites, Section 3 contains rock-magnetic data and Section 4 contains the magnetic fabric data of all specimens presented in stereonet as well as in tables.

REFERENCES

Airoldi, G., Muirhead, J.D., White, J.D.L. & Rowland, J., 2011. Emplacement of magma at shallow depth: insights from field relationships at Allan Hills, south Victoria Land, East Antarctica, *Antarct. Sci.,* **23,** 281–296

Almqvist, B.S.G., Bosshard, S.A., Hirt, A.M., Mattsson, H.B. & Hetényi, G., 2012. Internal flow structures in columnar jointed basalt from Hrepphólar, Iceland: II. Magnetic anisotropy and rock magnetic properties, *Bull. Volcanol.,* **74**(7), 1667–1681.

Anderson, D.L., 2000. The thermal state of the upper mantle; No role for mantle plumes, *Geophy. Res. Lett.,* **27**(22), 3623–3626.

Archanjo, C.J. & Launeau, P., 2004. Magma flow inferred from preferred orientations of plagioclase of the Rio Ceara-Mirim dyke swarm (NE Brazil) and its AMS significance, *Geol. Soc. London Spec. publ.,* **238,** 285–298.

Aubourg, C., Giordano, G., Mattei, M. & Speranza, F., 2002. Magma flow in sub-aqueous rhyolitic dikes inferred from magnetic fabric analysis (Ponza Island, W. Italy), *Phys. Chem. Earth, Parts A/B/C,* **27,** 1263–1272.

Baksi, A.K., 1995. Petrogenesis and timing of volcanism in the Rajmahal flood basalt province, northeastern India, *Chem. Geol.,* **121,** 73–90.

Bian, W., Yang, T., Ma, Y., Jin, J., Gao, F. & Wang, S., 2019. Paleomagnetic and geochronological results from the Zhela and Weimei formations lava flows of the eastern Tethyan Himalaya: new insights into the breakup of eastern Gondwana, *J. geophys. Res. Solid Earth,* **124**(1), 44–64.

Black, B.A. & Manga, M., 2017. Volatiles and the tempo of flood basalt magmatism, *Earth planet. Sci. Lett.,* **458,** 130–140.

Caballero-Miranda, C.I., Alva-Valdivia, L.M., González-Ranzel, J.A., Gogitchaishvili, A., Urrutia-Fucugauchi, J. & Kontny, A., 2016. Vertical AMS variation within basalt flow profiles from the Xitle volcano (Mexico) as indicator of heterogeneous strain in lava flows, *J. Volc. Geotherm. Res.,* **31,** 19–28.

Callot, J.-P. & Geoffroy, L., 2004. Magma flow in the East Greenland dyke swarm inferred from study of anisotropy of magnetic susceptibility: magmatic growth of a volcanic margin, *Geophys. J. Int.,* **159**(2), 816–830.

Cañón-Tapia, E. & Herrero-Bervera, E., 2009. Sampling strategies and the anisotropy of magnetic susceptibilities of dykes, *Tectonophysics,* **466,** 3–17.

Cañón-Tapia, E., 2004. Anisotropy of magnetic susceptibility of lava flows and dykes: a historical account, in *Magnetic Fabric: Methods and Applications,* Geological Society Special Publications, Vol. 238, pp. 205–225, eds Martin-Hernández, F., Lüneburg, C.M., Aubourg, C. & Jackson, M., Geol. Soc. London.

Chadima, M. & Jelínek, V., 2008. Anisoft 4.2.—Anisotropy data browser, *Contributions to Geophysics and Geodesy, Special Issue,* **38,** 38–41.

Chadima, M., Cajz, V. & Týcová, P., 2009. On the interpretation of normal and inverse magnetic fabric in dikes. Examples from the Eger Graben, NW Bohemian Massif, *Tectonophysics,* **466,** 47–63.

Coffin, M.F., Pringle, M.S., Duncan, R.A., Gladezenko, T.P., Storey, M., Mqller, R.D. & Gahagan, L.A., 2002. Kerguelen hotspot magma output since 130 Ma, *J. Petrol.,* **43,** 1121–1139.

Constable, C. & Tauxe, L., 1990. The bootstrap for magnetic susceptibility tensors, *J. geophys. Res.,* **95,** 8383–8395.

Curtis, M.L., Riley, T.R., Owens, W.H., Leat, P.T. & Duncan., R.A., 2008. The form, distribution and anisotropy of magnetic susceptibility of Jurassic dykes in H.U. Sverdrupfjella, Dronning Maud Land, Antarctica: implications for dyke swarm emplacement, *J. Struct. Geol.,* **30,** 1429–1447.

Das, A. & Mallik, J., 2020. Applicability of AMS technique as a flow fabric indicator in dykes: insight from Nandurbar–Dhule Deccan dyke swarm, *Int. J. Earth Sci.,* **109**(3), 933–944.

Das, A., Mallik, J. & Banerjee, S., 2021. Characterization of the magma flow direction in the Nandurbar-Dhule Deccan dyke swarm inferred from magnetic fabric analysis, *Phys. Earth planet. Inter.,* **319,** 106782.

Day, R., Fuller, M. & Schmidt, V.A., 1977. Hysteresis properties of titanomagnetites: grain size and compositional dependence, *Phys. Earth Planet. Inter.,* **13**(4), 260–266.

de Wall, H., 2000. The field dependence of AC-susceptibility in titanomagnetites: implications for the anisotropy of magnetic susceptibility, *Geophys. Res. Lett.,* **27,** 2413–2416.

Delcamp, A., Petronis, M.S. & Troll, V.R., 2015. Discerning magmatic flow patterns in shallow-level basaltic dykes from the NE rift zone of Tenerife, Spain, using the anisotropy of magnetic susceptibility (AMS) technique, *Geol. Soc. London Spe. Publ.,* **396,** 87–106.

Dudzisz, K., Kontny, A. & Alva-Valdivia, L.M., 2022. Curie temperature and emplacement conditions of pyroclastic deposits from Popocatepetl colano, Mexico, *Geochem. Geophys. Geosys.,* **23,** 8.

Dunlop, D.J., 2002. Theory and application of the day plot (M_{rs}/M_s versus H_{cr}/H_c) 1. Theoretical curves and tests using titanomagnetite data, *J. geophys. Res.,* **104**(B3), 2056. doi: 10.1029/2001JB000486.

Egli, R., 2013. VARIFORC: an optimized protocol for the calculation of non-regular first-order reversal curve (FORC) diagrams, *Glob. Planet. Change,* **110,** 302–320.

Eriksson, P.I., Riiishuus, M.S., Sigmundsson, F. & Elming, S.-A., 2011. Magma flow directions inferred from field evidence and magnetic fabric studies of the Streitishvarf composite dike in east Iceland, *J. Volc. Geotherm. Res.,* **206,** 30–45.

Eriksson, P.I., Riishuus, M.S. & Elming, S.A., 2014. Magma flow and palaeo-stress deduced from magnetic fabric analysis of the Álftafjördur dyke swarm: implications for shallow crustal magma transport in Icelandic volcanic systems, *Geol. Soc. Spe. Publ.,* **396,** 107–132.

Ernst, R.E. & Baragar, W.R.A., 1992. Evidence from magnetic fabric for the flow pattern of magma in the Mackenzie giant radiating dyke swarm, *Nature,* **356,** 511–513.

Ernst, R.E., 2014. *Large Igneous Provinces,* Cambridge University Press.

Ernst, R.E., Liikane, D.A., Jowitt, S.M., Buchan, K.L. & Blanchard, J.A., 2019. A new plumbing system framework for mantle plume-related continental Large Igneous Provinces and their mafic-ultramafic intrusions, *J. Volc. Geotherm. Res.,* **384,** 75–84.

Ferré, E., 2002. Theoretical models of intermediate and inverse AMS fabric, *Geophys. Res. Lett.,* **29**(7), 1127. doi: 10.1029/2001GL014367.

Fialko, Y.A. & Rubin, A.M., 1999. Thermal and mechanical aspects of magma emplacement in giant dike swarms, *J. geophys. Res.,* **104**(10), 23 033–23 049.

Geoffroy, L., Callot, J.P., Aubourg, C. & Moreira, M., 2002. Magnetic and plagioclase linear fabric discrepancy in dykes a new way to define the flow, *Terra Nova,* **14**(3), 183–190.

Ghatak, A. & Basu, A.R., 2011. The Sylhet Traps: vestiges of the Kerguelen plume in NE India, *Earth planet. Sci. Lett.,* **308,** 52–64.
Ghatak, A. & Basu, A.R., 2013. Isotopic and trace element geochemistry of alkalic–mafic–ultramafic–carbonatitic complexes and flood basalts in NE India: origin in a heterogeneous Kerguelen plume, *Geochim. Cosmochim. Acta,* **115,** 46–72.
Greenough, J.D. & Hodych, J.P., 1990. Evidence for lateral magma injection in the early mesozoic dykes of eastern North America, in *Mafic Dykes and Emplacement Mechanisms,* pp. 35–46, eds Parker, A.J., Rickwood, P.C. & Tucker, D.H., A.A. Balkema
Gudmundsson, A., 1990. Dyke emplacement at divergent plate boundaries, in *Mafic Dykes and Emplacement Mechanisms,* pp. 47–62, eds Parker, A.J., Rickwood, P.C. & Tucker, D.H., A.A. Balkema.
Gudmundsson, A., 2002. Emplacement and arrest of sheets and dykes in central volcanoes, *J. Volc. Geotherm. Res.,* **116,** 279–298.
Harrison, R.J. & Feinberg, J.M., 2008. FORCinel: an improved algorithm for calculating first-order reversal curve distributions using locally weighted regression smoothing, *Geochem. Geophys. Geosyst.,* **9,** Q05016.
Hastie, W.W., Watkeys, M.K. & Aubourg, C., 2011. Significance of magnetic and petrofabric in Karoo-feeder dykes, northern Lebombo, *Tectonophysics,* **513,** 96–111.
Holtzman, B.K., Kohlstedt, D.L. & Morgan, J.P., 2005. Viscous energy dissipation and strain partitioning in partially molten rocks, *J. Petrol.,* **46,** 2569–2592. http://dx.doi.org/10. 1093/petrology/egi065.
Hrouda, F., 1982. Magnetic anisotropy of rocks and its application in geology and geophysics, *Surv. Geophys.,* **5**(1), 37–82.
Hrouda, F., 2011. Models of frequency-dependent susceptibility of rocks and soils revisited and broadened, *Geophys. J. Int.,* **187,** 1259–1269.
Hrouda, F., Chadima, M. & Ježek, J., 2022. Anisotropy of out-of-phase magnetic susceptibility and its potential for rock fabric studies: a review, *Geoscience,* **12,** 234.
Hrouda, F., Chadima, M., Ježek, J. & Pokorny, J., 2017. Anisotropy of out-of-phase magnetic susceptibility of rocks as a tool for direct determination of magnetic subfabrics of some minerals: an introductory study, *Geophys. J. Int.,* **208,** 385–402.
Hrouda, F., Faryad, S.W., Kubinova, Š., Verner, K. & Chlupačova, M., 2019. Simultaneous free flow and forcefully driven movement of magma in lamprophyre dykes as indicated by magnetic anisotropy: case study from the Central Bohemian Dyke Swarm, Czech Republic, *Geoscience,* **104**.
Hrouda, F., Ježek, J. & Chadima, M., 2020. Anisotropy of out-of-phase magnetic susceptibility as a potential tool for distinguishing geologically and physically controlled inverse magnetic fabrics in volcanic dykes, *Phy. Earth planet. Inter.,* **307,** 106551.
Huppert, H.E. & Sparks, R.S.J., 1989. Chilled margins in igneous rocks, *Earth planet. Sci. Lett.,* **92,** 397–405.
Jackson, M. & Bowles, J., 2018. Malleable Curie temperatures of natural titanomagnetites: occurrences, modes, and mechanisms, *J. geophys. Res. Sol. Earth,* **123,** 921–940.
Jelinek, V., 1981. Characterization of the magnetic fabric of rocks, *Tectonophysics,* **79,** T63–T67.
Kapawar, M.R., Venkateshwarlu, M. & Sangode, S.J., 2021. Anisotropy of magnetic susceptibility study to locate the feeder zone and lava flow directions of the Rajmahal Traps (India): implications to Kerguelen mantle plume interaction with Indian plate, *Phy. Earth planet. Inter.,* **313**.
Kent, R.W., Pringle, M.S., Müller, R.D., Saunders, A.D. & Ghose, N.C., 2002. $^{40}Ar/^{39}Ar$ geochronology of the Rajmahal Basalts, India, and their relationship to the Kerguelen Plateau, *J. Petrol.,* **43**(7), 1141–1153.
Kent, R.W., Saunders, A.D., Kempton, P.D. & Ghose, N.C., 1997. Rajmahal basalts, eastern India: mantle source and melt distribution at a volcanic rifted margin, in *Large Igneous Provinces—Continental, Oceanic and Planetary Flood Volcanism,* Geophysical Monograph Series, pp. 145–182, eds Mahoney, J.T. & Coffin, M.F., American Geophysical Union.
Khan, M.A., 1962. The anisotropy of magnetic susceptibility of some igneous and metamorphic rocks, *J. geophys. Res.,* **67,** 2873–2885.
Kissel, C., Laj, C., Sigurdsson, H. & Guillou, H., 2010. Emplacement of magma in eastern Iceland dikes: insights from magnetic fabric and rock magnetic analysis, *J. Volc. Geotherm. Res.,* **191,** 79–92.
Knight, M.D. & Walker, G.P.L., 1988. Magma flow directions in dikes of the Koolau Complex, Oahu, determined from magnetic fabric studies, *J. geophys. Res.,* **93,** 4301–4319.
Kosterov, A., Conte, G., Goguitchaichvili, A. & Urrutia-Fucugauchi, J., 2009. Low-temperature magnetic properties of andesitic rocks from Popocatepetl stratovolcano, Mexico, *Earth Planets Space,* **61**(1), 133–142.
Kumar, A. & Ahmad, T., 2007. Geochemistry of mafic dykes in part of Chotanagpur gneissic complex: petrogenetic and tectonic implications, *Geochem. J.,* **41,** 173–186.
Kusbach, V.K., Machek, M., Roxerová, Z., Racek, M. & Silva, P.F., 2019. Localization effect on AMS fabric revealed by microstructural evidence across small-scale shear zone in marble, *Sci. Rep.,* **9,** 17483.
Lied, P., Kontny, A., Nowaczyk, N., Mrlina, J. & Kämpf, H., 2020. Cooling rates of pyroclastic deposits inferred from mineral magnetic investigations: a case study from the pleistocene Mýtina Maar (Czech Republic), *Int. J. Earth Sci.,* **109,** 1707–1725.
Lowrie, W., 1990. Identification of ferromagnetic minerals in a rock by coercivity and unblocking temperature properties, *Geophy. Res. Lett.,* **17,** 159–162.
Mahoney, J.J. & Coffin, M.F., 1997. *Large Igneous Provinces: Continental, Oceanic, and Planetary Flood Volcanism,* American Geophysical Union.
Mahoney, J.J., Macdougall, J.D., Lugmair, G.W. & Gopalan, K., 1983. Kerguelen hotspot source for Rajmahal Traps and Ninetyeast Ridge?, *Nature,* **303**(5916), 385–389.
Mantiloni, L., Rivalta, E. & Davis, T., 2023. Mechanical modeling of pre-eruptive magma propagation scenarios at Calderas, *J. geophys. Res. Sol. Earth,* **128,** e2022JB025956.
Martin, S.A., Kavanagh, J.L., Biggin, A.J. & Utley, J.E.P., 2019. The origin and evolution of magnetic fabrics in mafic sills, *Front. Earth Sci.,* **7,** 1–23.
Mattsson, H.B., Caricchi, L., Almqvist, B.S.G., Caddick, M.J., Bosshard, S.A., Hetényi, G. & Hirt, A.M., 2011. Melt migration in basalt columns driven by crystallization-induced pressure gradients, *Nat. Commun.,* **2**(1), 1–6.
Maxbauer, D.P., Feinberg, J.M. & Fox, D.L., 2016. MAX UnMix: a web application for unmixing magnetic coercivity distributions, *Comput. Geosci.,* **95,** 140–145.
Mittal, T. & Richards, M.A., 2021. The magmatic architecture of continental flood basalts 2: a new conceptual concept, *J. geophys. Res. Solid Earth,* **126**(12), e2021JB021807.
Moreira, M.A., Geoffroy, L. & Pozzi, J.P., 2015. Magma flow pattern in dykes of the Azores revealed by anisotropy of magnetic susceptibility, *J. geophys. Res. Solid Earth,* **120,** 662–690.
Morgan, W.J., 1981. Hotspot tracks and the opening of the Atlantic and Indian Oceans, in *The Sea, Seventh edn.,* eds Emiliani, C., John Wiley & Sons.
Olierook, H.K.H., Jourdan, F., Merle, R.E., Timms, N.E., Kusznir, N. & Muhling, J.R., 2016. Bunbury Basalt: gondwana breakup products or earliest vestiges of the Kerguelen mantle plume?, *Earth planet. Sci. Lett.,* **440,** 20–32.
Pan, X., Shen, Z., Roberts, P.A., Heslop, D. & Shi, L., 2014. Syntectonic emplacement of late cretaceous mafic dyke swarms in coastal southeastern China: insights from magnetic fabrics, rock magnetism and field evidence, *Tectonophysics,* **637,** 328–340.
Patil, S.K. & Arora, B.R., 2008. Palaeomagnetic and rock magnetic studies on the intrusives from Raniganj Basin, Damodar Valley: linkage to the Rajmahal volcanics, in *INDIAN DYKES: Geochemistry, Geophysics and Geochronology,* pp. 511–526, eds Srivastava, R.K., Sivaji, C. & Chalapathi Rao, N.V., Narosa Publishing House Pvt Ltd.
Peng, W., Yang, T., Shi, Y., Bian, W., Ma, Y. & Wang, S., 2022. Role of the Kerguelen mantle plume in breakup of eastern Gondwana: evidence

from early cretaceous volcanic rocks in the eastern Tethyan Himalaya, *Palaeogeogr. Palaeoclimatol. Palaeoecol.,* **588**.
Philpotts, A.R. & Dickson, L.D., 2000. The formation of plagioclase chains during convective transfer in basaltic magma, *Nature,* **406,** 59–61..
Raposo, M.I.B. & D'agrella-Filho, M.S., 2000. Magnetic fabrics of dike swarms from SE Bahia State, Brazil: their significance and implications for mesoproterozoic basic magmatism in the São Francisco Craton, *Precambrian Res.,* **99,** 309–325.
Raposo, M.I.B. & Ernesto, M., 1995. Anisotropy of magnetic susceptibility in the Ponta Grossa dyke swarm (Brazil) and its relationship with magma flow direction, *Phy. Earth planet. Inter.,* **87,** 183–196.
Raposo, M.I.B., D'agrella-Filho, M.S. & Pinese, J.P.P., 2007. Magnetic fabrics and rock magnetism of archaean and proterozoic dike swarms in the southern São Francisco Craton, Brazil, *Tectonophysics,* **443** , 53–71.
Rasband, W.S., 2012. ImageJ: image processing and analysis in Java, record ascl:1206.013 .
Ray, J.S., Pattanayak, S.K. & Pande, K., 2005. Rapid emplacement of the Kerguelen plume–related Sylhet Traps, eastern India: evidence from ^{40}Ar-^{39}Ar geochronology, *Geophy. Res. Lett.,* **32**(10), L10303.
Ray, R., Sheth, H.C. & Mallik, J., 2007. Structure and emplacement of the Nandurbar–Dhule mafic dyke swarm, Deccan Traps, and the tectonomagmatic evolution of flood basalts, *Bull. Volcanol.,* **69,** 537–551.
Rivalta, E., Taisne, B., Bunger, A.P. & Katz, R.F., 2015. A review of mechanical models of dike propagation: schools of thought, results and future directions, *Tectonophysics,* **638,** 1–42.
Roberts, A.P., Pike, C.R. & Verosub, K.L., 2000. First-order reversal curve diagrams: a new tool for characterizing the magnetic properties of natural samples, *J. geophys. Res.,* **105,** 28 461–28 475.
Rochette, P., Jackson, M. & Aubourg, C., 1992. Rock magnetism and the interpretation of anisotropy of magnetic susceptibility, *Rev. Geophys.,* **30**(3), 209–226.
Shajahan, R., Harris, A., Mana, S., Nicotra, E., Test, C.R., Vries, B.V.W. & Zanella, E., 2024. Emplacement and flow dynamics in a small volcanic dyke swarm: the example of Mount Calanna (Etna, Italy), *J. Volc. Geotherm. Res.,* **449,** 108069. doi: 10.1016/j.jvolgeores.2024.108069.
Shukla, G., Mallik, J., Krishna, Y. & Banerjee, S., 2024. Late-stage Deccan eruption from multiple shallow magma chambers through vertical flow along fissures: insights from magnetic fabric analysis of the Panchmari dyke swarm, *Phy. Earth planet. Inter.,* **357,** 107285. doi: 10.1016/j.pepi.2024.107285.
Silva, P.F. *et al.* 2008. Magma flow, exsolution processes and rock metasomatism in the great Messejana–Plasencia dyke (Iberian Peninsula), *Geophy. J. Int.,* **175,** 806–824.
Silva, P.F., Marques, F.O., Machek, M., Henry, B., Hirt, A.M., Roxerová, Z., Madureira, P. & Vratislav, S., 2014. Evidence for non-coaxiality of ferrimagnetic and paramagnetic fabrics, developed during magma flow and cooling in a thick mafic dyke, *Tectonophysics,* **629,** 155–164.
Singh, A.P., Kumar, N. & Singh, B., 2004. Magmatic underplating beneath the Rajmahal Traps: gravity signature and derived 3-D configuration, *J. Earth Syst. Sci.,* **113**(4), 759–769.
Soriano, C., Amorós, E.B. & Crespo, M.G., 2007. Dike intrusion under shear stress: effects on magnetic and vesicle fabrics in dikes from rift zones of Tenerife (Canary Islands), *J. Struct. Geol.,* **29**(12), 1931–1942.
Soriano, C., Elisabet, B., Garcés, M. & Ort, M.H., 2016. 'Anomalous' magnetic fabric of dikes in the stable single domain/superparamagnetic threshold, *Geophy. J. Int.,* **204,** 1040–1059.
Srivastava, R.K., Guarino, V., Wu, F.-Y., Melluso, L. & Sinha, A.K., 2019b. Evidence of sub-continental lithospheric mantle sources and open system crystallization processes from in-situ U-Pb ages and Nd-Sr-Hf isotope geochemistry of the cretaceous ultramafic-alkaline-(carbonatite) intrusions from the Shillong Plateau, northeastern India, *Lithos,* **330–331,** 108–119.
Srivastava, R.K., Heaman, L.M., Sinha, A.K. & Shihua, S., 2005. Emplacement age and isotope geochemistry of Sung Valley alkaline–carbonatite complex, Shillong Plateau, northeastern India: implications for primary carbonate melt and genesis of the associated silicate rocks, *Lithos,* **81,** 33–54.
Srivastava, R.K., Kumar, S., Sinha, A.K. & Chalapathi Rao, N.V., 2014. Petrology and geochemistry of high-titanium and low-titanium mafic dykes from the Damodar valley, Chhotanagpur Gneissic Terrain, eastern India and their relation to mantle plume(s), *J. Asian Earth Sci.,* **84,** 34–50.
Srivastava, R.K., Sinha, A.K. & Kumar, S., 2012. Geochemical characteristics of mesoproterozoic metabasite dykes from the Chhotanagpur gneissic terrain, eastern India: implications for their emplacement in a plate margin tectonic environment, *J. Earth Syst. Sci.,* **121** , 509–523.
Srivastava, R.K., Wang, F. & Shi, W., 2020. Substantiation of R´eunion plume induced prolonged magmatic pulses (ca. 65.5–70.5 Ma) of the Deccan LIP in the Chhotanagpur Gneissic Complex, eastern India: constraints from ^{40}Ar/^{39}Ar geochronology, *J. Earth Syst. Sci.,* **129,** 96.
Srivastava, R.K., Wang, F., Shi, W. & Ernst, R.E., 2023. Early cretaceous mafic dykes from the Chhota Nagpur gneissic terrane, eastern India: evidence of multiple magma pulses for the main stage of the Greater Kerguelen mantle plume, *J. Asian Earth Sci.,* **241,** 105464. 10.1016/j.jseaes.2022.105464.
Srivastava, R.K., Wang, F., Shi, W., Sinha, A.K. & Buchan, K.L., 2019a. Nature of cretaceous dolerite dikes with two distinct trends in the Damodar Valley, eastern India: constraints on their linkage to mantle plumes and large igneous provinces from ^{40}Ar/^{39}Ar geochronology and geochemistry, *Lithosphere,* **12**(1), 40–52.
Stephenson, A., 1994. Distribution anisotropy: two simple models for magnetic lineation and foliation, *Phys. Earth planet. Inter.,* **82,** 49–53.
Storey, M. *et al.* 1992. Lower cretaceous rocks in continental margins and their relationship to the Kerguelen Plateau, in *Proceedings of the Ocean Drilling Program, Scientific Results, Vol. 120,* pp. 33–53. Available at: https://www-odp.tamu.edu/publications/120_SR/VOLUME/CHAPTERS/sr120_02.pdf.
Tarling, D.H. & Hrouda, F., 1993. *The Magnetic Anisotropy of Rocks,* Chapman & Hall, 217pp.
Tibaldi, A., 2015. Structure of volcano plumbing systems: a review of multi-parametric effects, *J. Volc. Geotherm. Res.,* **298,** 85–135.
Trippanera, D., Porreca, M., Urbani, S., Kissel, C., Winkler, A., Sagnotti, L., Nazzareni, S. & Acocella, V., 2020. Interpreting inverse magnetic fabric in miocene dikes from eastern Iceland, *J. geophy. Res. Sol. Earth,* **125**(11), e2020JB020306.
Wiegand, M., Trumbull, R.B., Kontny, A. & Greiling, R.O., 2017. An AMS study of magma transport and emplacement mechanisms in mafic dykes from the Etendeka Province, Namibia, *Tectonophysics,* **716** , 149–167.
Woo, J.Y.L. & Kilburn, C.R.J., 2010. Intrusion and deformation at Campi Flegrei, southern Italy: sills, dikes, and regional extension, *J. geophy. Res.,* **115,** B12210.
Zhang, Q. & Appel, E., 2023. Reversible thermal hysteresis in heating-cooling cycles of magnetic susceptibility: a fine particle effect of magnetite, *Geophy. Res. Lett.,* **50,** e2023GL102932.
Zhu, D.-C., Chung, S.-L., Mo, X.-X., Zhao, Z.-D., Niu, Y., Song, B. & Yang, Y.-H., 2009. The 132 ma Comei-Bunbury large igneous province: remnants identified in present-day southeastern Tibet and southwestern Australia, *Geology,* **37**(7), 583–586.